



Future projection of the African easterly waves in a high-resolution atmospheric general circulation model

Jerry Raj¹ · Hamza Kunhu Bangalath^{1,2} · Georgiy Stenchikov¹

Received: 31 March 2022 / Accepted: 14 February 2023
© The Author(s) 2023

Abstract

Simulating the features of the African Easterly Waves (AEWs), such as their westward propagation off the east Atlantic coast, is challenging for coarse-resolution climate models. In this study, we use High-Resolution Atmospheric Model (HiRAM) to simulate AEWs and analyze their future projections by the end of the twenty first century. The simulations are performed globally at a horizontal resolution of ~ 25 km. The model uses shallow convective parameterization for moist convection and stratiform cloudiness. Future projections are conducted using representative concentration pathway 8.5. The AEWs are separated with respect to their periods as 3–5- and 6–9-day period AEWs, and bandpass filtering is used to filter the waves from the mean flow. HiRAM simulates structure and propagation of the waves well; however, it tends to overestimate the associated precipitation. In the future, the AEW precipitation and intensity of the circulation will considerably increase. The northward extent of the AEW track also shows a significant increase in the future. Enhanced baroclinic overturning and eddy available potential energy generated due to diabatic heating is also observed in the future.

Keywords African easterly waves · High resolution GCM · Future projection

1 Introduction

The African easterly waves (AEWs) are responsible for the high-frequency variability of West African Monsoon (WAM) precipitation (Duvel 1990; Diedhiou et al 1998; Mathon et al 2002; Gu et al 2004; Mekonnen et al 2006) and most of the total annual rainfall over the Sahel (Fink and Reiner 2003; Barbe and Lebel 1997; D’Amato and Lebel 1998; Laurent et al 1998; Redelsperger et al 2002; Fink et al 2006). AEWs are westward-moving synoptic scale disturbances over tropical Africa and the Atlantic (CARLSON 1969; Burpee 1974). They are seed disturbances for cyclogenesis in the tropical Atlantic (Landsea 1993; Pasch et al

1998) and are instrumental in transporting Saharan dust semiglobally. They can be detected at 600–700 hPa on either side of the African Easterly Jet (AEJ) (Reed et al 1988; Chen 2006; Pytharoulis and Thorncroft 1999). There are two types of AEWs: AEWs with periods of 3–5 and 6–9 days. Over West Africa, the 3–5 day AEWs follow two tracks centered over 5°N and 15°N , which eventually merge over 17.5°N in the tropical Atlantic (Crétat et al 2015). The 6–9 day AEWs can be found north of AEJ at around 17.5°N (Diedhiou et al 1998; Wu et al 2013). These two types of AEWs differ in the wavelength, propagation speed, and rainfall pattern they produce. The 3–5 day AEWs have an average wavelength of 3000 km and 5000 km over the north and south of AEJ, respectively; whereas the 6–9 day AEWs have longer wavelengths of 5000–6000 km. The southern track AEWs have a phase speed of approximately 12 m/s, whereas the northern track waves are slower with a phase speed of 7–8 m/s (De Felice et al 1990; Diedhiou et al 1998). For the 3–5 day AEWs, convection is found ahead and in phase with the trough while they are on land and shifts to behind the trough when they reach the ocean; whereas positive precipitation anomalies are found behind the trough for the 6–9 day AEWs (Diedhiou et al 1998). Many earlier studies associated the formation of AEWs with an unstable AEJ (Burpee

✉ Jerry Raj
jerry.raj@kaust.edu.sa

Hamza Kunhu Bangalath
hkb2@nyu.edu

Georgiy Stenchikov
georgiy.stenchikov@kaust.edu.sa

¹ Earth Science and Engineering, King Abdullah University of Science and Technology, Thuwal, Saudi Arabia

² Center for Prototype Climate Modeling, New York University Abu Dhabi, Abu Dhabi, United Arab Emirates

1972; Reed et al 1977; Norquist et al 1977; Albignat and Reed 1980; Thorncroft and Hoskins 1994a). However, recent studies have argued that AEWs are initiated by pre-existing convection over east Africa (Berry and Thorncroft 2005; Lin 2004; Mekonnen et al 2006; Kiladis et al 2006).

AEWs are a major control of West African rainfall and the associated Mesoscale Convective Systems (MCSs) and squall lines embedded within them. More than 40% of the total MCSs over the region are associated with AEWs and these MCSs account for approximately 80% of the total annual rainfall over the Sahel (Fink and Reiner 2003; Barbe and Lebel 1997; D'Amato and Lebel 1998; Laurent et al 1998; Redelsperger et al 2002; Fink et al 2006). Approximately 60% of all Atlantic hurricanes and 80% of major hurricanes have their genesis associated with AEWs (Landsea 1993; Pasch et al 1998; Russell et al 2017), even though not all of the hurricanes in this region are formed from AEWs. Southern track AEWs are more likely to develop into hurricanes, whereas northern track AEWs contain less moisture than their southern counterparts and are consequently less efficient in their contribution to tropical cyclogenesis (Chen 2006). The variability of AEWs have impacts on the rainfall of West Africa, through MCSs, and on the climate along their tracks in the Atlantic, through cyclogenesis. Thus the future projection of AEWs is of utmost importance in regards to these two regions.

Skinner and Diffenbaugh (2014) used CMIP5 models to quantify the response of AEWs to increased radiative forcing. Their study shows increased AEW strength toward the north of AEJ (15°–25°N), whereas southern track AEWs do not exhibit a robust response by the end of the twenty first century. Martin and Thorncroft (2015) also used CMIP5 models to analyze the future projection of AEWs and found large differences in responses of high- and low-resolution models. In their study, AEW activity exhibits a reduction in late spring and early summer and a higher intensity between July and October. Hannah and Aiyer (2017) used the super-parameterized community earth system model (SP-CESM), with an embedded cloud-resolving model, to study AEW activity in quadrupled CO₂ experiments. In their study, an increase in baroclinicity causes the northern wave track to be more active while a reduction of the occurrence of weak waves and a slight increase in the occurrence of strong waves is seen along the southern track. A similar result was reported by Brannan and Martin (2019) in their study of AEW tracks. A contrasting result of reduction of AEW activity throughout the region was reported by Kebe et al (2020) in their study using Regional Climate Model 4 (RegCM4). Similarly Mariotti et al (2014) also reported a reduction in 6–9 day AEW activity by the end of the century.

AEWs are convectively initiated in east and central Africa, and the topography of this region, especially the Ethiopian highlands, Marra Mountain, and Guinea

Highlands, play a significant role in their initiation and propagation (Hamilton et al 2020). Therefore, the horizontal resolution of the model is a crucial constraint in the simulation of AEWs. Coarse-resolution models are found to be unable to propagate AEWs off the coast toward the Atlantic (Martin and Thorncroft 2015). The diminished westward propagation of AEWs in these models could be owing to the inability of low-resolution models to resolve Guinea Highlands. The convection and diabatic heating over Guinea Highlands are instrumental in reinvigorating the AEWs and in assisting them to propagate off the coast. Skinner and Diffenbaugh (2014) found that coarse-resolution models in CMIP5 are unable to simulate distinct northern and southern AEW tracks. Furthermore, simulating rainfall over West Africa is challenging for coarse-resolution models since it involves multiscale processes and is influenced by complex topography and coastlines. However, Martin and Thorncroft (2015) hypothesized that enhancing resolved topography alone might be insufficient to improve the representation of AEWs in models and that convective parameterization also plays a major role in the simulation of AEWs.

Energy conversion terms associated with the development and intensification of AEWs are particularly sensitive to the parameterizations used. Models with crude latent heat parameterization (Rennick 1976) and prescribed mean state of AEJ (Thorncroft and Hoskins 1994a, b) have found that barotropic energy conversion associated with the shear of AEJ is the main energy source of AEWs. Meanwhile, diabatic heating is identified as the major energy source of AEWs when a model with prescribed cumulus convective heating of the intertropical convergence zone (ITCZ) is used (Estoque and Lin 1977). Hsieh and Cook (2007) found that the baroclinic conversion associated with meridional overturning is the main energy source in their study using a Regional Climate Model (RCM) with parameterized convection. They also found that moist convection on the southern side AEJ increases barotropic conversion via strengthening the wind shear, which in turn enhances the baroclinic conversion and induces resonance. All of the aforementioned studies have analyzed only the 3–5 day AEWs. Diedhiou et al (2002) used reanalysis data to estimate the energy conversion terms for both 3–5 and 6–9 day AEWs and found that major energy sources of these two waves are different. According to their study, the main energy source of the 3–5 day AEWs is the barotropic conversion, whereas the 6–9 day AEWs grow through both barotropic and baroclinic conversions below the jet core.

In this study, we use an atmospheric general circulation model (AGCM)–high-resolution atmospheric model (HiRAM)–to explore the changes in AEW activity by the end of the twenty first century. High-resolution GCMs are effective in overcoming several limitations encountered by coarse-resolution GCMs. Due to their fine grid-spacing,

important processes, such as large-scale condensation, land-sea interaction, and topographical forcing, are better resolved in high-resolution GCMs (Boyle and Klein 2010). Studies suggest that with increasing horizontal resolution, GCMs are better able to explicitly capture MCSs (e.g. Zhao et al 2009; Manganello et al 2012), reproduce diurnally forced circulations, represent orographically modulated rainfall (e.g. Boyle and Klein 2010; Lau and Ploshay 2009), and represent extreme precipitation events (Wehner et al 2014). Since they can resolve mesoscale processes, multiscale interactions are better represented in high-resolution GCMs (Gent et al 2010). HiRAM, the high-resolution AGCM used in this study, does not parameterize deep convection instead uses a six-category bulk cloud microphysics scheme for the resolved component of cumulus convection processes (Zhao et al 2009). We assume that this could also improve the representation of AEWs in the model. Few studies in the past investigated the changes in energetics associated with AEW response to warming. This study gives a special emphasis on the changes in energetics of future AEWs.

The objective of this study is to examine the future changes in AEWs with increased greenhouse gas emissions and analyze the causes of these changes. The first part of the study comprises model validation and examination of how well the AEWs are represented in the model. In the second part, the future projection of the AEWs, which uses the Representative Concentration Pathway (RCP) 8.5 is analyzed. A brief review of the model and a detailed description of the experiment setting follows the introduction. The summary and a discussion of the results conclude the paper.

2 Model and experimental setup

We used an experiment setup identical to that used by Raj et al (2019) which used the same model, HiRAM, to analyze the future changes to the WAM system. HiRAM was developed at the Geophysical Fluid Dynamics Laboratory (GFDL) (Zhao et al 2009; GAMDT 2004), based on the atmospheric component (AM2) of the GFDL coupled model 2 (CM2). It uses a cubed-sphere finite-volume dynamical core (Putman and Lin 2007; Lin 2004), and the simulations are conducted at C360 (25 km) horizontal resolution. This horizontal resolution is comparable to that of the regional climate downscaling. HiRAM uses a shallow convective scheme for moist convection and stratiform cloudiness (Bretherton et al 2004) which makes the contribution of the resolved vertical transport more significant, especially in the tropics. Global aerosol forcing is incorporated as monthly climatologies of the five aerosol species (i.e., dust, black carbon, organic carbon, sulfate, and sea salt) (Ginoux et al 2006), which are precalculated using the global chemistry transport model, Model for OZone And Related chemical

Tracers (MOZART) (Horowitz et al 2003). The representation of dust is crucial because the radiative forcing caused by it is essential for an accurate simulation of the north African summer climate (Bangalath and Stenchikov 2015, 2016). The simulations cover the entire globe, but we restrict the analysis to the West African domain in this study. The model is coupled to the GFDL Land Model 3, and a prescribed model equilibrium seasonal vegetation climatology and prescribed sea surface temperatures (SSTs) are used.

The history period simulation uses SST from ESM2M, the Earth System Model (ESM) developed at GFDL, which uses GFDL's Modular Ocean Model (MOM) (Dunne et al 2012, 2013). This simulation is named HiRAM ESM2M and spans a period of 30 years, from 1975 to 2004. To evaluate the model performance, ERA5 reanalysis (Hersbach et al 2020) and NASA GPM IMERG satellite-based precipitation data (Hou et al 2014) are used. Precipitation data from ERA Interim reanalysis (Dee et al 2011) and GPCP (Adler et al 2018) are used to compare observation and reanalysis datasets. The process-based evaluation of WAM elements was documented in (Raj et al 2019) and the comparison of mean precipitation and mean state of different WAM elements with observation can be found in the mentioned study.

To estimate the future changes of AEW, three ensemble simulations, starting from different initial conditions are conducted for the period 2076–2099 using the RCP 8.5 emission scenario. The anomalies of future projections are estimated with respect to 1985–2004 as the reference period from the historical simulations, and the statistical significance of the anomalies is estimated using the two-tailed student's *t*-test. The SST in the RCP 8.5 HiRAM simulation of 2076–2099 is obtained from ESM2M RCP8.5 simulations for the same period.

3 Results

There is significant discrepancy among various datasets in their representation of AEWs. Figure 1 shows the standard deviations of the bandpass-filtered precipitation for both 3–5 day and 6–9 day AEWs from four different datasets. Satellite observations from NASA IMERG (Fig. 1b, f) exhibits largest amount of precipitation followed by GPCP (Fig. 1a, e). Both ERA Interim (Fig. 1c, g) and ERA5 (Fig. 1d, h) reanalyses underestimate precipitation. It should be noted that ERA5 is better in reproducing AEW rainfall when compared with ERA Interim data in tropical Atlantic but it underestimates the rainfall over the continent. Precipitation in NASA IMERG and GPCP spread more westward and poleward indicating a wider wave propagation. But in both ERA5 and ERA Interim reanalyses the zonal and meridional extent of the rainbelt is less than the observations, indicating a much weaker wave activity than in the observations. We

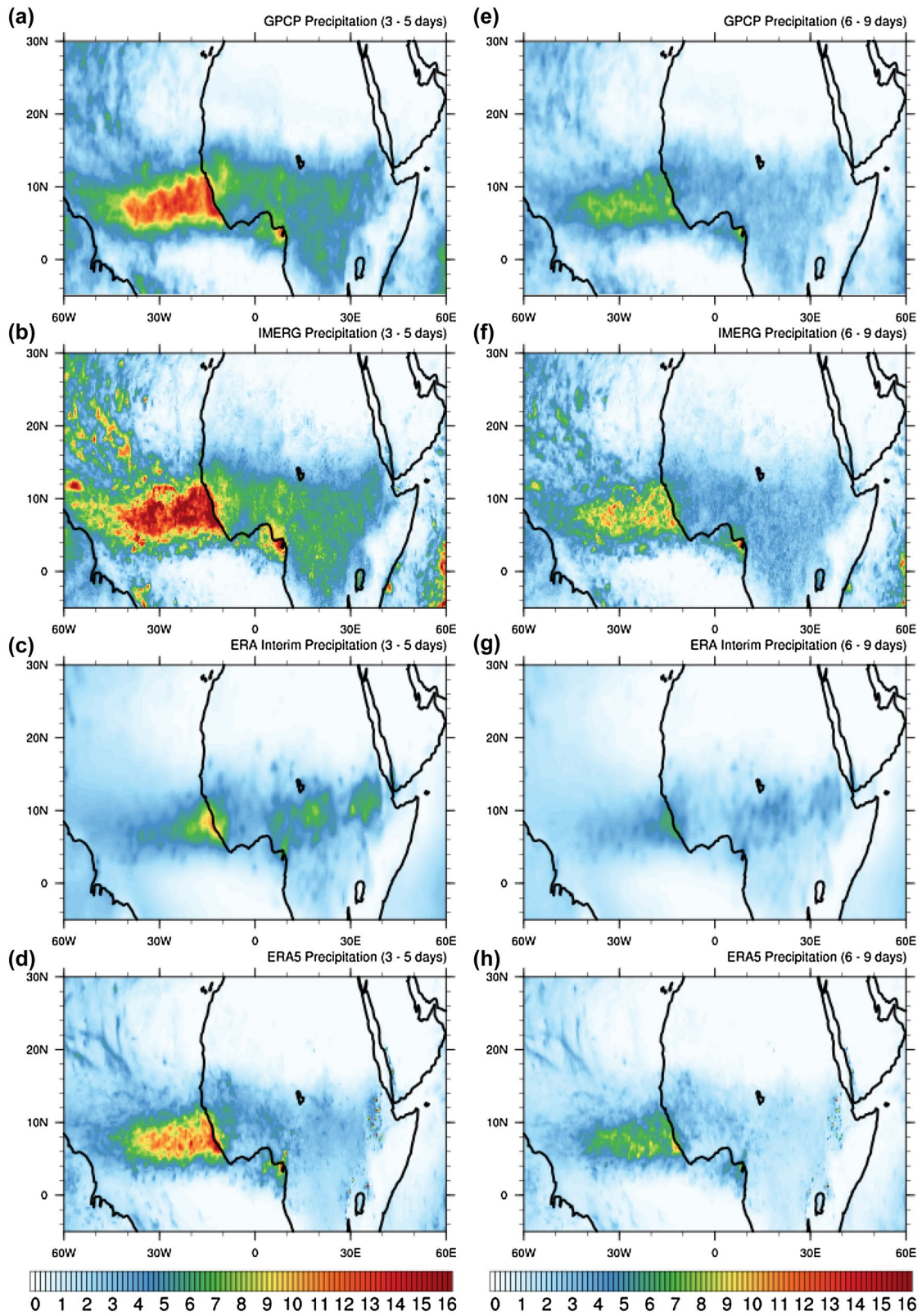


Fig. 1 Standard deviations of bandpass-filtered values of JJAS daily precipitation (mm/day) **a** GPCP 3–5 days, **b** NASA IMERG 3–5 days, **c** ERA Interim 3–5 days **d** ERA5 3–5 days, (**e–h**) similar to (**a–d**) except for 6–9 days

chose NASA IMERG precipitation data, and OLR and wind fields from ERA5 reanalyses to validate the model since they relatively better represent AEW precipitation.

To identify AEW activity, we calculated the zonal wave-number–frequency power spectra of the symmetric and asymmetric components of daily outgoing longwave radiation (OLR) following the methodology of Wheeler and Kiladis (1999) (Fig. 2). The spectra are normalized by the red background to differentiate the important power peaks from the background. The normalization also helps to avoid systematic biases while comparing different models or reanalyses since the power spectra of each dataset are displayed with respect to its own climatological variance. The black

lines are the hypothetical dispersion curves in a shallow water mode corresponding to different depths. In general, all power peaks of HiRAM are close to the respective hypothetical dispersion curves and the signals compare very well with those of ERA5. AEWs are observed as the dominant spectral peaks associated with a westward wave number between 6 and 20 (frequency) and period of 3–10 days (Gu et al 2004; Kiladis et al 2006), which were also identified as tropical depressions (Wheeler and Kiladis 1999). AEW signals are evident in ERA5 and HiRAM simulations. However, the power associated with AEWs is overestimated in HiRAM ESM2M compared with ERA5 data (Figs. 2c, d) indicating more intense wave activity.

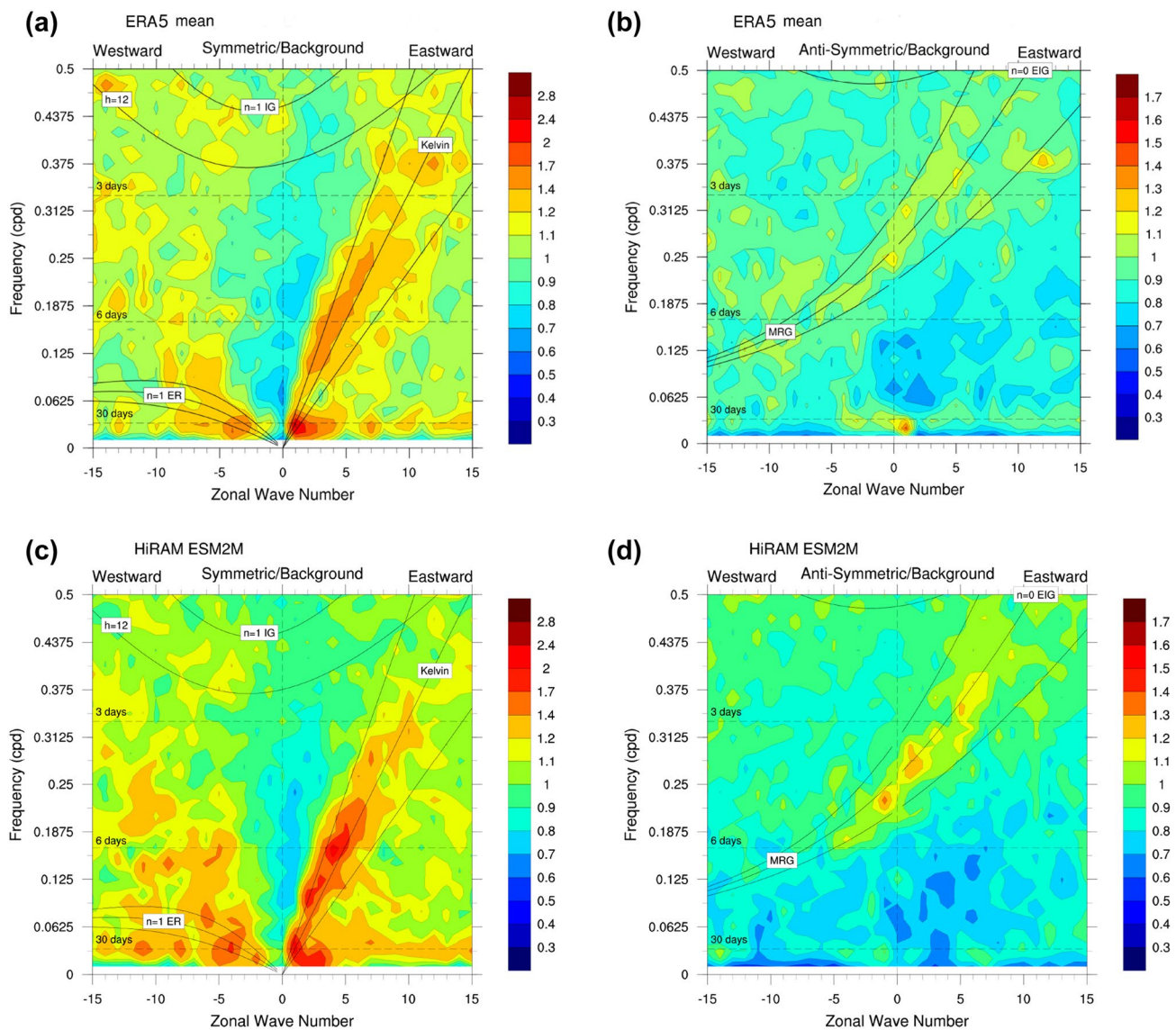


Fig. 2 Wavenumber–frequency power spectra of OLR for June–August 1979–1984, averaged from 15°N to 15°S, plotted as the ratio of the raw OLR spectrum against a smooth red noise background, for the symmetric component from **a** ERA5 **c** HiRAM ESM2M and for

the asymmetric component from **b** ERA5 **d** HiRAM ESM2M. Solid lines are dispersion curves for Kelvin, equatorial Rossby (ER), mixed Rossby-gravity (MRG), and inertio-gravity (IG) waves

To analyze the mean characteristics associated with the 3–5 day AEWs in both reanalysis data and HiRAM, standard deviations of 3–5 day bandpass-filtered values of OLR, meridional wind at 700 hPa, and precipitation for the June, July, August, and September (JJAS) season are examined (Fig. 3). The standard deviation of bandpass-filtered daily OLR represents the variability of the synoptic-scale convective activity associated with 3–5 day AEWs (Fig. 3a, b). A band of convective activity stretches from Ethiopian highlands to tropical Atlantic, and this band's position shifts more equatorward once it reaches the Atlantic Ocean. On the continental part, this band is located slightly north of the WAM rain belt, whereas it is collocated with the ITCZ over the marine parts of the domain. The HiRAM ESM2M simulation overestimates the variability of the synoptic-scale convective activity, and the band is not as well defined as in ERA5 data (Fig. 3a). Most enhanced activities are found over the land and the northward extent reaches up to 20°N. The HiRAM overestimates climatological mean convection (Raj et al 2019), and part of this enhanced convection arises from the amplified variability of the synoptic-scale convective activity. Figure 3c shows the variability of the 700 hPa meridional wind from the reanalysis data. A band of high variability extends northward from the Western Sahel to the Atlantic at 20°N. This band is collocated with the AEW tracks. HiRAM ESM2M simulation accurately reproduces the location of this band; however, the simulated variability of the meridional wind is stronger than that in ERA5 data (Fig. 3d). Figures 3e and f show the 3–5 day variability of precipitation in IMERG data and HiRAM ESM2M simulation, respectively. The variability of precipitation is collocated with that of the synoptic-scale convective activity, as expected (Fig. 3e). HiRAM reproduces the 3–5 day rainfall variability comparable to IMERG data, although the former slightly overestimates the variability over land region.

Figure 4 is the same as Fig. 3, except for the 6–9 day AEWs. The OLR variability is at the same location as that of the 3–5 day AEWs, except with a diminished intensity (Fig. 4a). The 6–9 day AEWs are located at the northern flank of AEJ in a drier location, and hence, their contribution to convection is less than that of the southern track AEWs. Similar to the 3–5 day AEWs, HiRAM ESM2M overestimates the OLR variability by $\approx 6 \text{ W/m}^2$ (Fig. 4b) over land. Compared with the 3–5 day AEWs, the mid-level meridional wind variability is located farther north (Fig. 4c). The wind variability simulated by HiRAM is comparable to that in ERA5 (Fig. 4d) although the high variability band extends more equatorward in the HiRAM simulation. The contribution to precipitation variability by 6–9 day AEWs is less than 3–5 day AEWs, as expected (Fig. 4e). However, HiRAM overestimates precipitation variability, especially over the marine ITCZ region (Fig. 4f). The observed overestimation of the variability in the precipitation and associated fields,

such as OLR, can be because HiRAM permits smaller-scale organized convection. The convective parameterization used in HiRAM is less intrusive and the model does not have parameterization for deep convection (Zhao et al 2009). Therefore, considerable differences between the synoptic- or subsynoptic-scale variability between ERA5 and HiRAM are expected. Studies that used superparameterization also showed similar differences between model and reanalyses (McCrary et al 2014).

4 Structure of AEWs

We extracted AEWs from the mean field using the Butterworth bandpass-filtered meridional wind at 700 hPa. The 700 hPa level is used by several studies to identify and analyze AEWs (CARLSON 1969; Berry and Thorncroft 2005, 2012; Kiladis et al 2006). The composite anomalies for the first day of wave (0th day) are constructed from the wind and rainfall anomalies associated with the highest and lowest decile of the bandpass-filtered 700 hPa meridional wind at an anchor location. The anchor location for 3–5 day AEWs is 1°W and 11.5°N and for 6–9 day AEWs is 1°W and 17.5°N. Similarly, we calculated circulation and precipitation anomalies for -4 , -2 , $+2$, $+4$ days for both types of AEWs. A similar method was used by Cr  tat et al (2015) to calculate the composite anomalies. Figure 5a–e show the mean evolution of 3–5 day AEWs from -4 to $+4$ days and the rainfall associated with them. The wind field is from ERA5 reanalysis data and the precipitation anomalies are from NASA IMERG data. A clear wave structure can be seen in figures corresponding from -2 to $+2$ days. The wavelength is approximately 3000 km, and the northern extent reaches well into Sahara. The rainfall anomalies are concentrated in the southern part of the wave core. The positive rainfall anomalies are located near northerly flow, ahead of the trough, whereas the negative rainfall anomalies are located to the south of the ridge, near the southerlies. The strongest winds are located around 5°W on all days. As the wave propagates into the Atlantic it moves more northward. It is also evident that the troughs and ridges exhibit a north-easterly tilt as they progress.

Figure 5f–j show the mean evolution of 3–5 day AEWs and the associated rainfall from the HiRAM ESM2M simulation. On -4 and -2 days the circulation and rainfall anomalies are overestimated in the simulation when compared with those in ERA5 data. This overestimation reduces as the wave progresses. Also, the troughs and ridges are more defined in the HiRAM simulation and the wavelength in the simulation is comparable with that in the reanalysis data. The negative and positive rainfall anomalies are located at the core, slightly southward, of ridges and troughs, respectively. It should also be noted that the

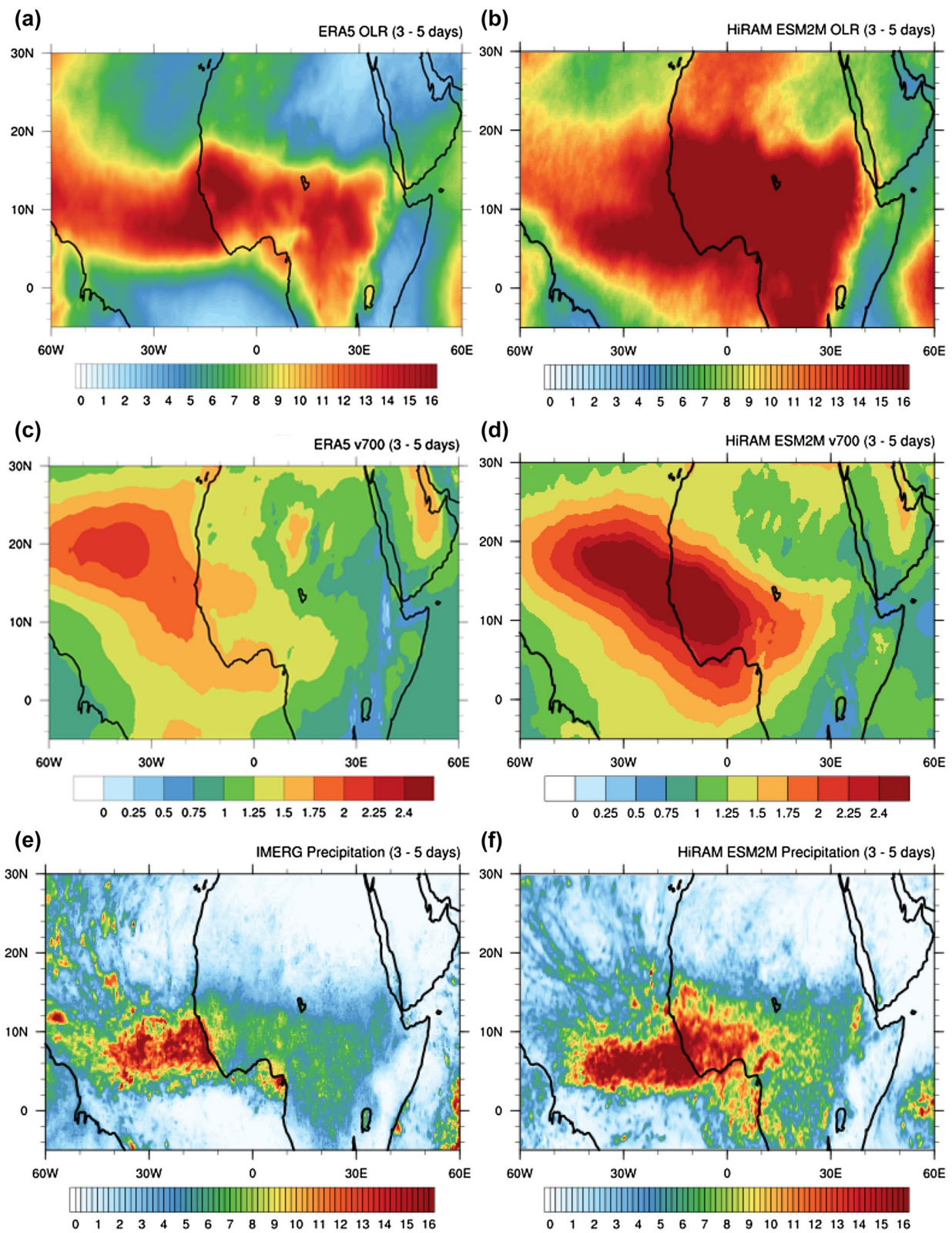


Fig. 3 Standard deviations of 3–5 day bandpass-filtered values of JJAS daily OLR (W/m^2) **a** ERA5, **b** HiRAM ESM2M, meridional wind at 700 hPa (m/s), **c** ERA5, **d** HiRAM ESM2M, and precipitation (mm/day), **e** NASA IMERG data, and **f** HiRAM ESM2M from 1979 to 2004

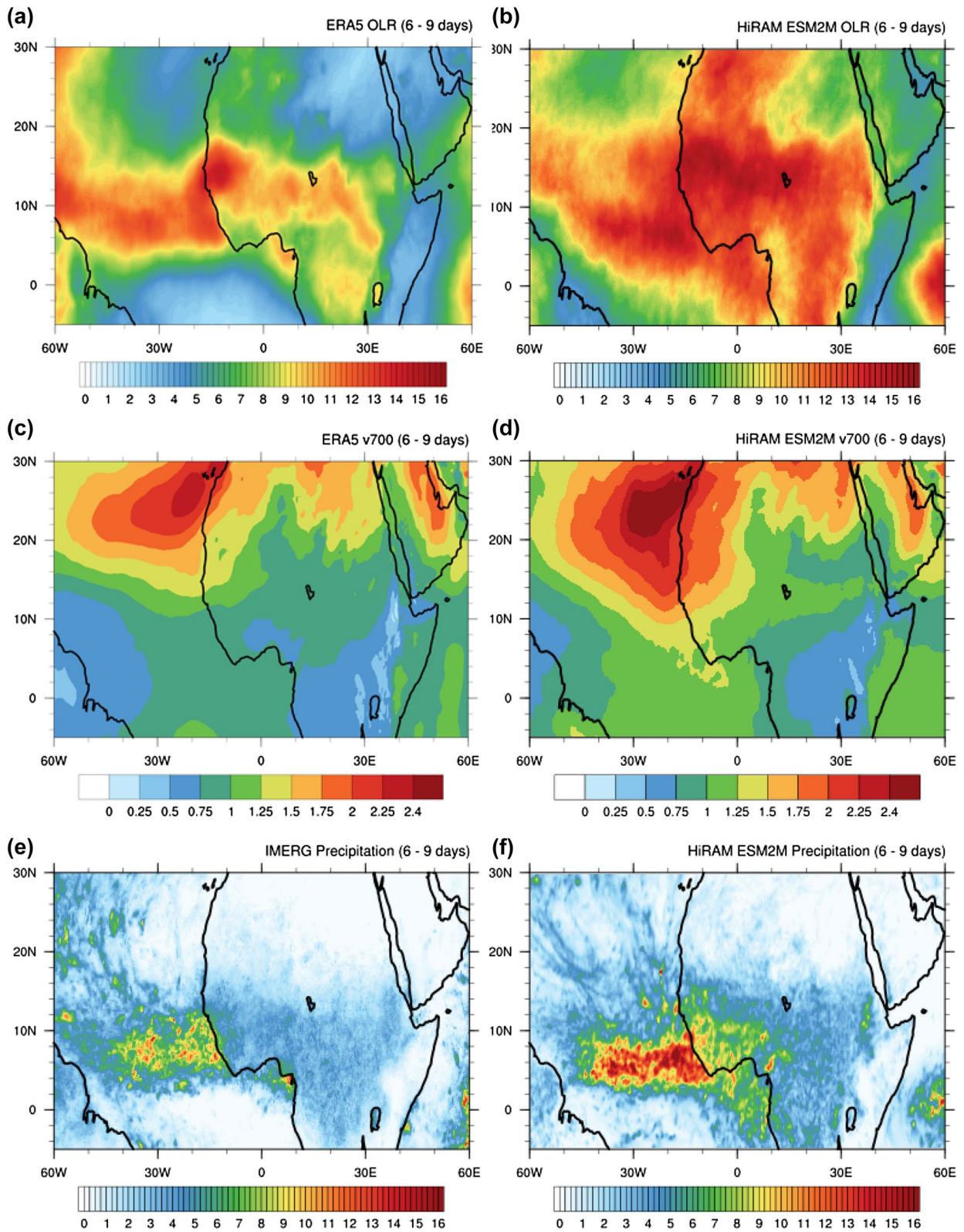


Fig. 4 Same as Fig. 2 but for 6–9 day bandpass filter

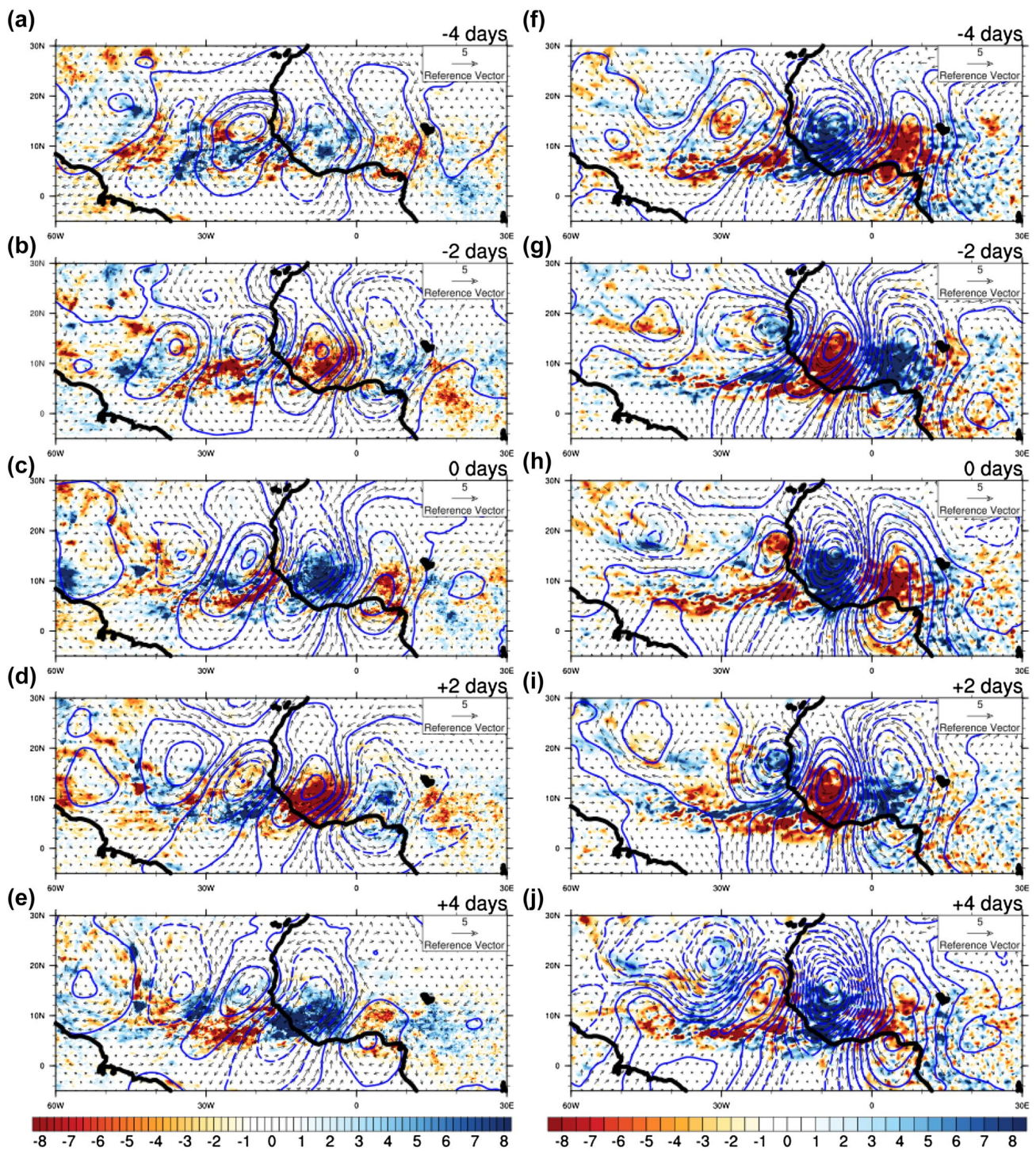


Fig. 5 Composite anomalies for 3–5-day AEWs from – 4 to +4 days for **a–e** IMERG precipitation and ERA5 wind field data and **f–j** HiRAM ESM2M simulation from 1979 to 2004. Vectors are 700 hPa

wind anomalies (m/s). Blue contours are the stream function. Rainfall anomalies (mm/day) are shaded

northward extent of the rainfall anomalies is also greater in the HiRAM simulation than in the reanalysis, and the Sahel experiences enhanced rainfall on the 0th day.

Figure 6 is the same as Fig. 5, except it shows the mean evolution of circulation and rainfall of 6–9 day AEWs. From Fig. 6a–e, which show the wave characteristics from

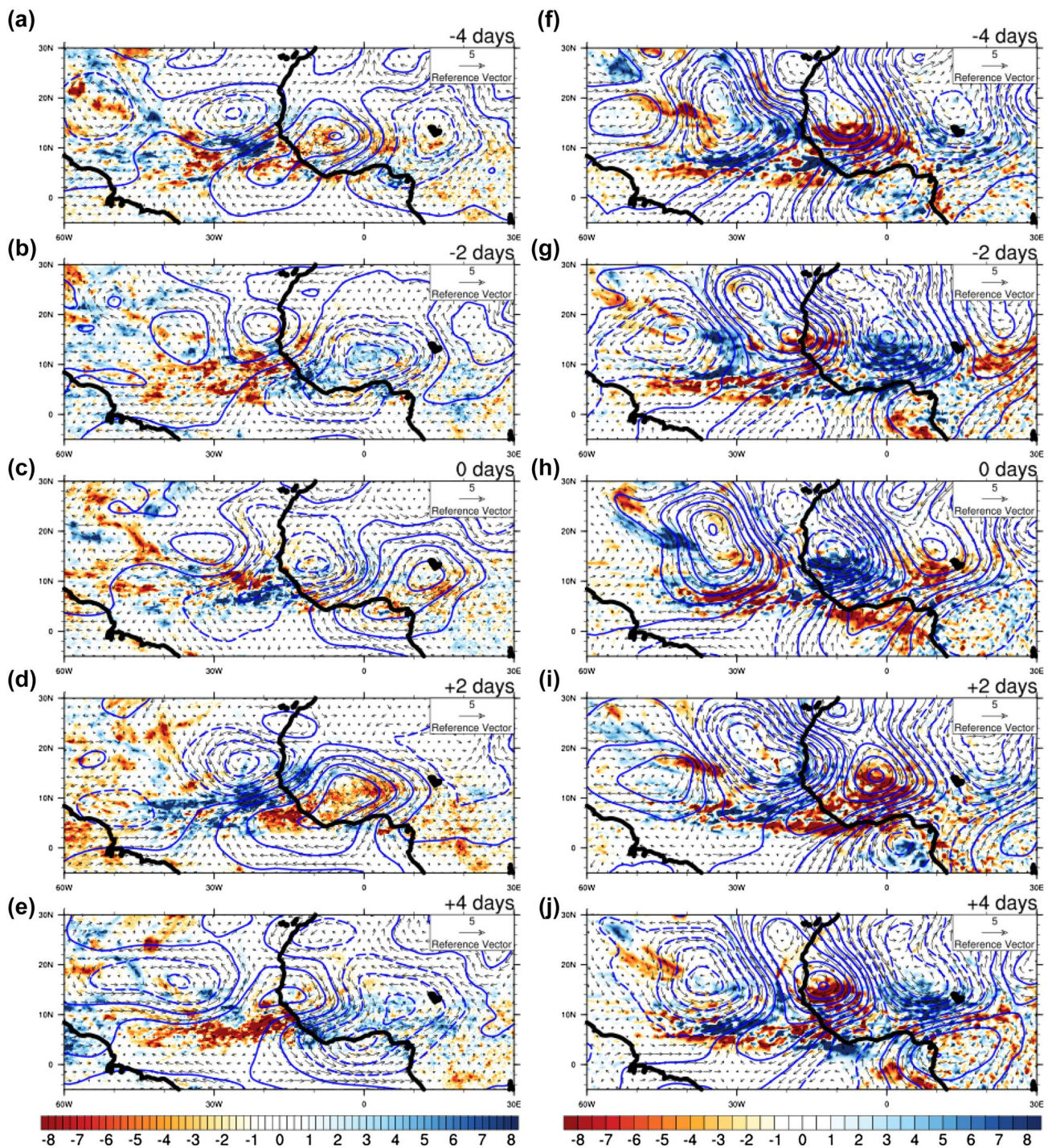


Fig. 6 Same as Fig. 4 but for 6–9 day AEWs

ERA5 data, it is evident that the 6–9 day AEWs have a longer wavelength (≈ 4500 km) than the 3–5 day AEWs as expected and their wave core is centered around 15°N . The rainfall anomalies are located at the southern edge of the wave train and are smaller in magnitude than those in the 3–5 day AEWs. A north–south dipole pattern of rainfall

anomalies is observed with negative anomalies along the Guinean coast and positive anomalies along the Sahel before the passing of the wave. This pattern is reversed after the wave passes, on +4 days. This dipole pattern is observed in the previous studies as well (Diedhiou et al

1998; Cr  tat et al 2015). The troughs and ridges exhibit a northeastward tilt in this case too.

Figure 6f–j show the mean evolution of circulation and rainfall anomalies associated with the 6–9 day AEWs in the HiRAM ESM2M simulation. The overall structure and location of the waves are similar to those in the reanalysis. The model overestimates both wind speed and rainfall, as in the case of the 3–5 day waves. The wavelength of the simulated 6–9 day AEWs is similar to that of the reanalysis data, which shows that although the precipitation is overestimated, the dynamic field agrees well with the observations. The southward extent of the rainfall anomalies is larger in the HiRAM simulation than in the reanalysis data; in particular, the Gulf of Guinea experiences larger rainfall anomalies. The dipole pattern over the Guinean coast and Sahel is reproduced by the model. The simulated 6–9 day AEWs exhibit a stronger circulation pattern than the simulated 3–5 day AEWs. The disagreement in the intensity of precipitation between the reanalysis data and model simulation could be attributed to the constrain arising from the weak and inconsistent data assimilation in the reanalysis (Trenberth et al 2001). Another reason could be the overzealousness of the convective parameterization used in the model. Notably, the westward propagation of the waves does not diminish in HiRAM as they reach the oceanic region. In general, GCMs struggle

to maintain their wave structure over the Atlantic. Moreover, for HiRAM, we observe a steady westward propagation.

Figure 7a, b show the meridional height cross-section of meridional wind on the 0th day associated with the 3–5 day AEWs from ERA5 and HiRAM ESM2M simulation respectively. Westerly wave propagation is evident in ERA5 and HiRAM, with a shift between northerly and southerly flows as the time progresses (Fig. S1). Vertically, the meridional wind anomaly exhibits a typical first baroclinic mode structure, with the meridional wind changing its direction at approximately 300 hPa. However, the wind structure has an eastward tilt from the surface to approximately 700 hPa and a westward tilt aloft. The tilt in the meridional wind structure (horizontal wind shear) indicates the presence of significant barotropic energy conversion. HiRAM simulates the propagation of the wave and the vertical and horizontal wind shears associated with the mixed barotropic–baroclinic process, consistent with the reanalysis (Fig. 7b). Our simulation agrees with previous studies (Burpee 1974; Kiladis et al 2006). However, the model marginally overestimates the magnitude of the wind. The wind reversal in the vertical happens in HiRAM at a higher level (200 hPa) than the ERA5 (300 hPa).

Figure 7c, d are similar to Fig. 7a, b, except for the 6–9 day day wave on the northern flank of the AEJ. As in the case of

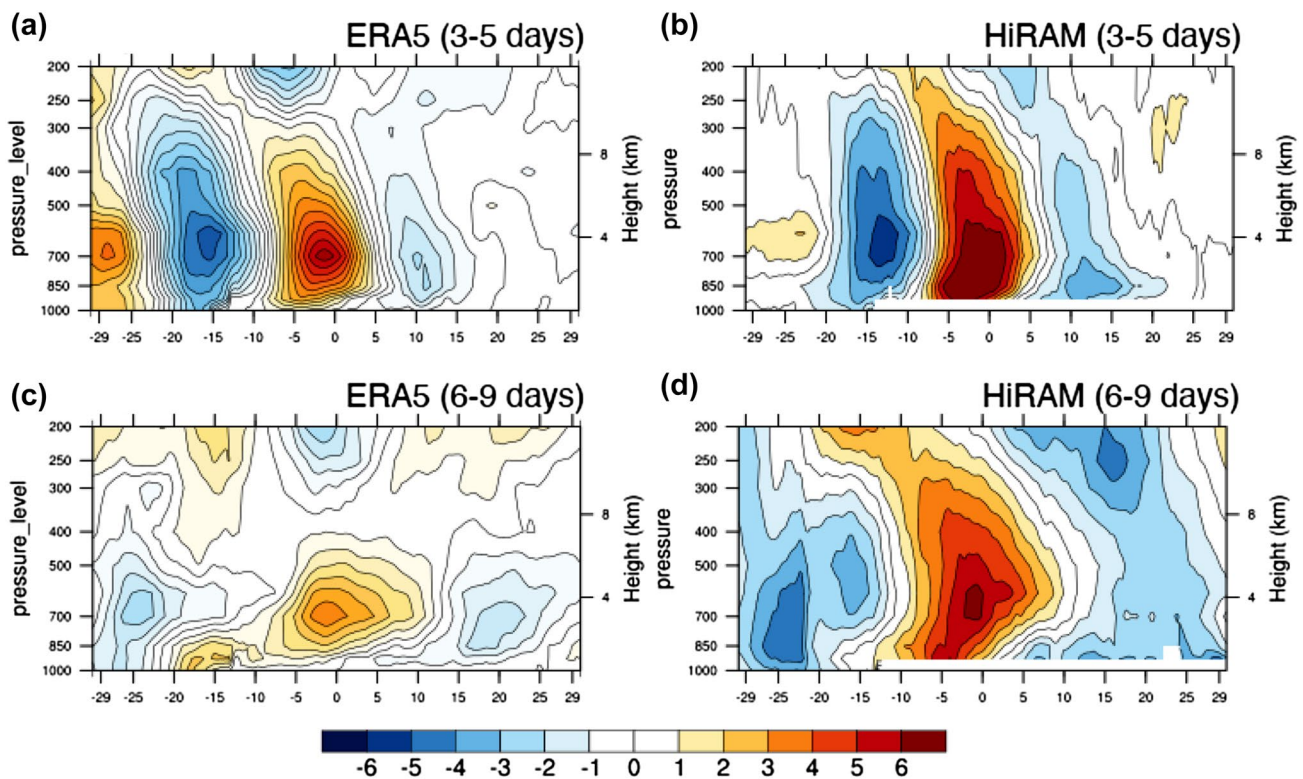


Fig. 7 Meridional height cross-sections of meridional wind (m/s) on 0th day for 3–5 day AEWs **a** ERA5 **b** HiRAM ESM2M and for 6–9 day AEWs **c** ERA5 **d** HiRAM ESM2M

the 3–5 day AEWs, HiRAM reproduces the wave propagation consistent with the reanalysis (Fig. S2). The first baroclinic mode in the vertical and the barotropic conversion associated with the wind shear is also reproduced. However, the eastward tilt in the lower troposphere and the westward tilt above it are more pronounced in the 6–9 day AEWs. The pronounced wind shear indicates a more significant role of barotropic conversion in the 6–9 day wave than in the 3–5 day southerly counterpart. As in the case of 3–5 day AEWs, HiRAM overestimates the wind speed when compared with ERA5 data.

5 Eddy kinetic energy

To analyze the frequency of occurrence and the intensity of AEW activity, we used Eddy Kinetic Energy (EKE), following previous studies (e.g. Leroux et al 2010; Martin and Thorncroft 2015). EKE is calculated as follows: $EKE = (u'^2 + v'^2)/2$, where u' and v' are the bandpass-filtered anomalies of the daily u and v data, respectively. We calculated EKE for 700 and 850 hPa to analyze the mid- and low-level AEW activities, respectively. Furthermore, EKE at 850 hPa plays an important role in tropical cyclogenesis

(Gray 1968; Thorncroft and Hodges 2001; Hopsch et al 2007). EKE calculated for 3–5 day AEWs from both ERA5 and HiRAM simulation is shown in Fig. 8. In general, the model overestimates EKE at both 700 and 850 hPa compared with the reanalysis data. The largest biases are seen at lower levels (Fig. 8d) and over the land regions. HiRAM ESM2M underestimates EKE over northern Sahara at mid-level and overestimates EKE over Sahel and Guinean coast at both levels (Fig. 8c, d). According to the previous study, HiRAM overestimates JJAS rainfall Guinean coast (Raj et al 2019) and it is safe to assume that this bias emerges from enhanced AEW activity in the model over this region. It should also be noted that over Atlantic, the largest bias is seen at 17.5°N, which is the region where the southern and northern track AEWs merge.

HiRAM simulates EKE that is comparable with ERA5 for 6–9 day AEWs at both mid and low levels, though it slightly overestimates it (Fig. 9c, d). The bias is seen over Atlantic centered around 18°N at both levels. Notably, the 6–9 day AEWs have the lowest EKE at 850 hPa, but the model overestimates EKE at this level. Another region where the model overestimates the EKE is the western Sahel. In general, a band of positive EKE bias starting

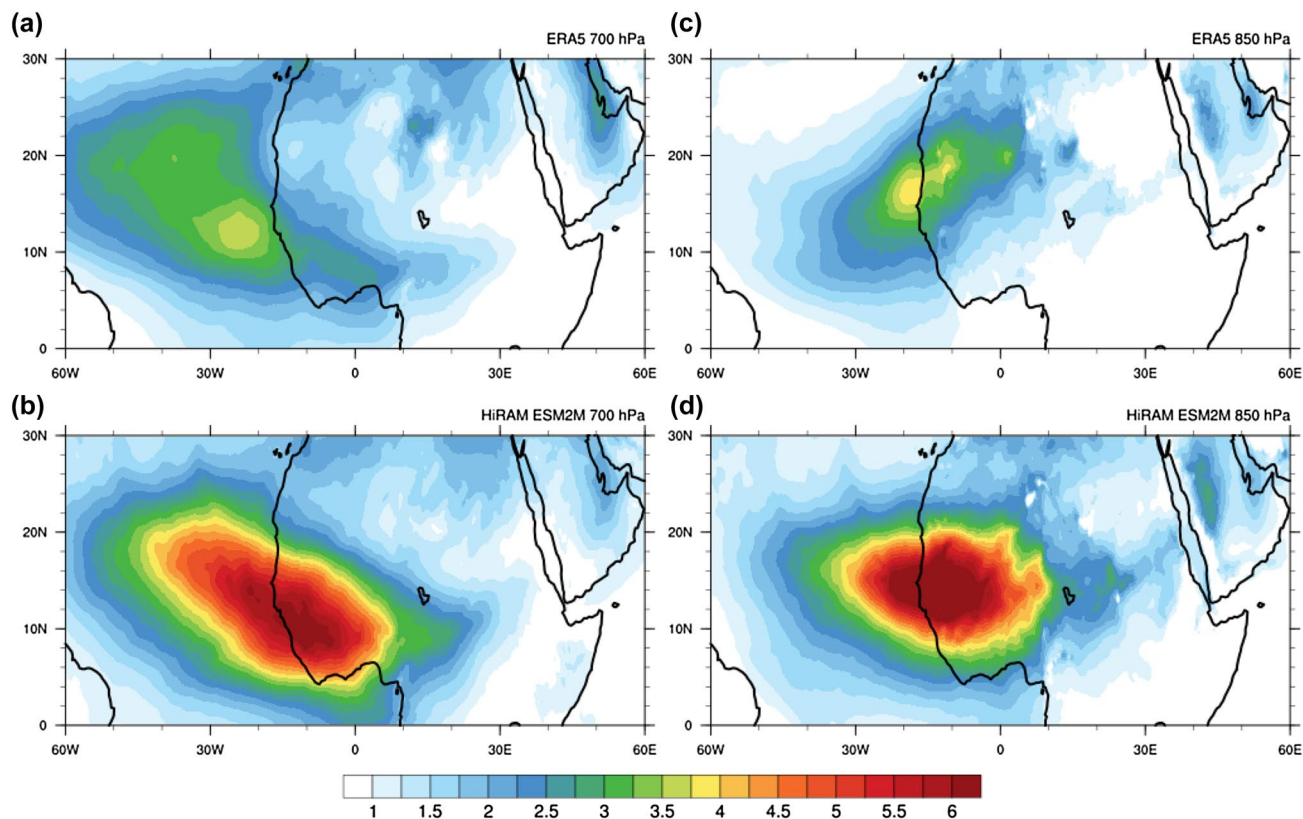


Fig. 8 EKE (m^2/s^2) of 3–5 day AEWs at 700 hPa for **a** ERA5 and **c** HiRAM ESM2M and at 850 hPa for **b** ERA5 and **d** HiRAM ESM2M from 1979 to 2004

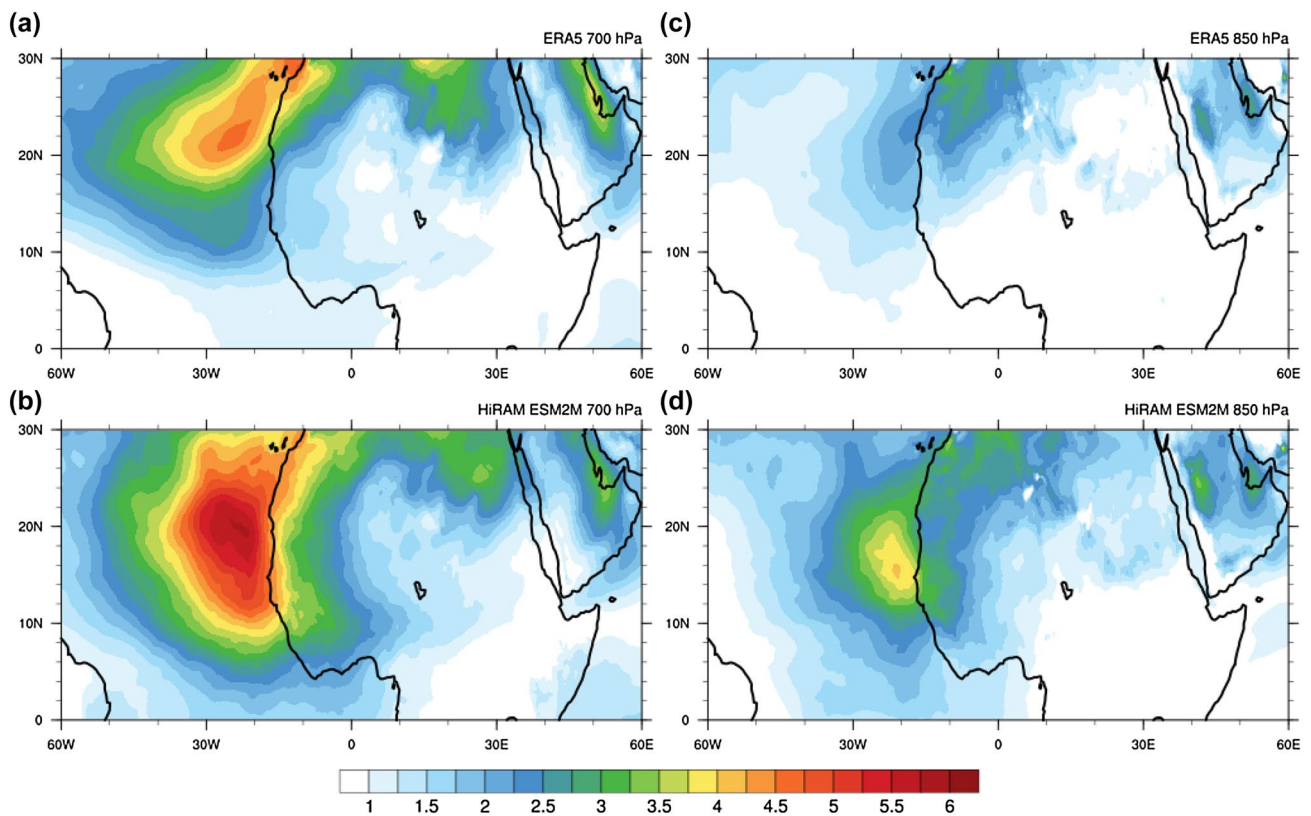


Fig. 9 Same as Fig. 6 but for 6–9 day AEWs

from the western Sahel to around 20°N in the Atlantic is seen in HiRAM simulations for both types of AEWs.

6 Future projection

Knowing how the AEW activity will change in the future is crucial because AEWs play a key role in the variability of Sahel rainfall and the genesis of Atlantic hurricanes. The zonal wavenumber–frequency power spectrum of the symmetric component of OLR from the HiRAM RCP 8.5 run shows that the power increases in the AEW region in the future, which indicates greater (more in number or stronger) activity (Fig. 10).

The standard deviation of precipitation anomaly between RCP 8.5 and history simulation for both 3–5 day and 6–9 day AEWs are shown in Fig. 11a, b respectively. For 3–5 day AEWs, there is a marked increase in precipitation over both continental and oceanic regions in the domain (Fig. 11a). The largest increase is observed over tropical Atlantic near Guinean coast while northern Atlantic also exhibits considerable increase in precipitation. Future precipitation anomaly for 6–9 day AEWs follow a similar pattern to that of 3–5 day AEWs (Fig. 11b). The largest anomalies are seen over the western coast as in the case of 3–5 day AEWs. Sahel

experiences an increase in precipitation for both types of AEWs.

Figures 12a, b show the mean circulation and precipitation anomalies for the 3–5 day AEWs from 2080 to 2099 simulated with RCP 8.5 on the 0th day for 3–5 day AEWs. In general, precipitation associated with the 3–5 day AEWs considerably changes, up to $|10|$ mm/day, in the future (Fig. 12b). Notably, the northward extent of the rain belt increases, reaching up to 20°N after the wave passes (fig. S3). The latitudinal extent of the circulation also increases, and the circulation intensity shows a marked increase. Moreover, the wave penetrates farther into the Atlantic, and the intensity in the marine region increases. Because AEWs sometimes act as the precursors of hurricanes, this could be translated as the tropical cyclone activity in the equatorial Atlantic may change in the future under this representative concentration pathway. Figure 12c, d show the mean circulation and precipitation anomalies of the 6–9 day AEWs. Similar to the 3–5 day AEWs, the 6–9 day AEWs exhibit an increase in the intensity of precipitation anomalies of approximately $|8|$ mm/day. The northward extent of these anomalies also increases by around 1° . The intensity of the circulation also increases. Remarkably, the circulation cell in the Atlantic becomes stronger and wider than the history simulation (Fig. S4).

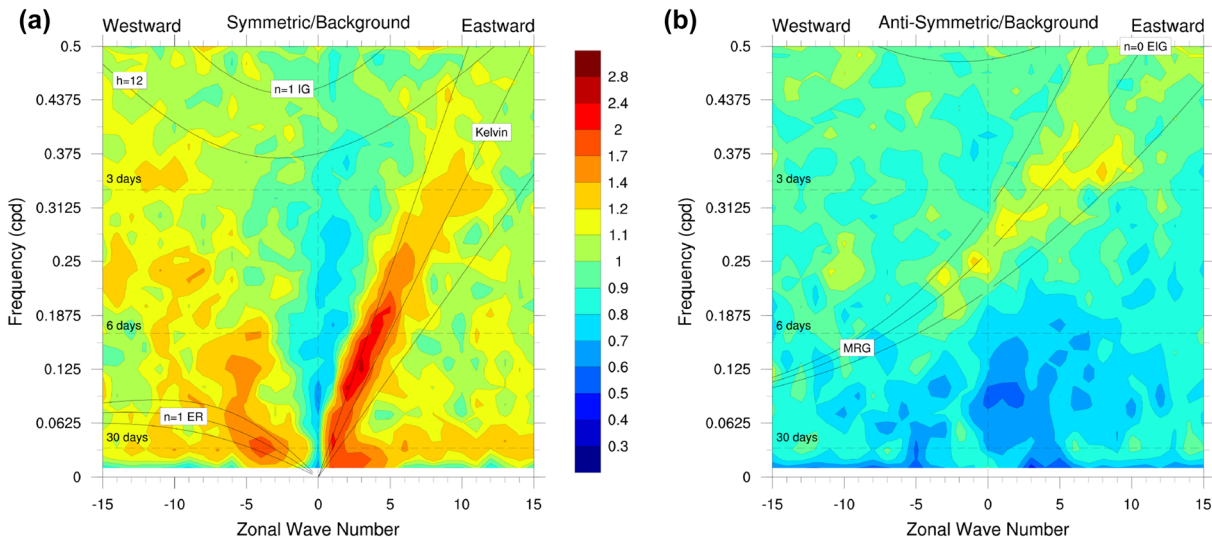


Fig. 10 Wavenumber–frequency power spectra of the symmetric component of OLR for June–August 2095–2099, averaged from 15°N to 15°S, plotted as the ratio of the raw OLR spectrum against

Figure 12e, f shows the meridional height cross-section of the anomalous (RCP8.5 - History) meridional wind on the 0th day days in RCP 8.5 projection, for the 3–5 day AEWs (left panel) and 6–9 day AEWs (right panel). In the 3–5 day AEWs, the first baroclinic mode associated with the deep convective heating is enhanced in the future. The oppositely flowing mid to lower and upper-tropospheric meridional winds are strengthening. The enhanced first baroclinic mode in the future agrees with the positive rainfall anomaly (Fig. 11) because the diabatic heating from deep convection latent heat release is the energy source for the baroclinic mode. Contrary to the 3–5 day case, the response to warming is weak in the 6–9 day waves. The first baroclinic mode structure is not significantly changed (fig. S5).

A change in EKE indicates a change in the number and/or intensity of AEW activity. By the end of the twenty first century, EKE of the 3–5 day AEWs shows a significant increase all over the domain. At 700 hPa level, a band of increased EKE spans from the Gulf of Guinea to around 50°W in the Atlantic (Fig. 13a). The northward extent of this band reaches up to 28°N. An increase of $\approx 1.8 \text{ m}^2/\text{s}^2$ is seen over the Gulf of Guinea and a slight increase is found over the western Sahel. A similar band of increased EKE is observed over the Atlantic at 850 hPa (Fig. 13d). However, at this level, in the Gulf of Guinea there is no visible increase in EKE, whereas in the Western Sahara and Sahel EKE increases up to $1.5 \text{ m}^2/\text{s}^2$. The enhanced EKE over the ocean indicates enhanced AEW amplitudes after they leave the coast.

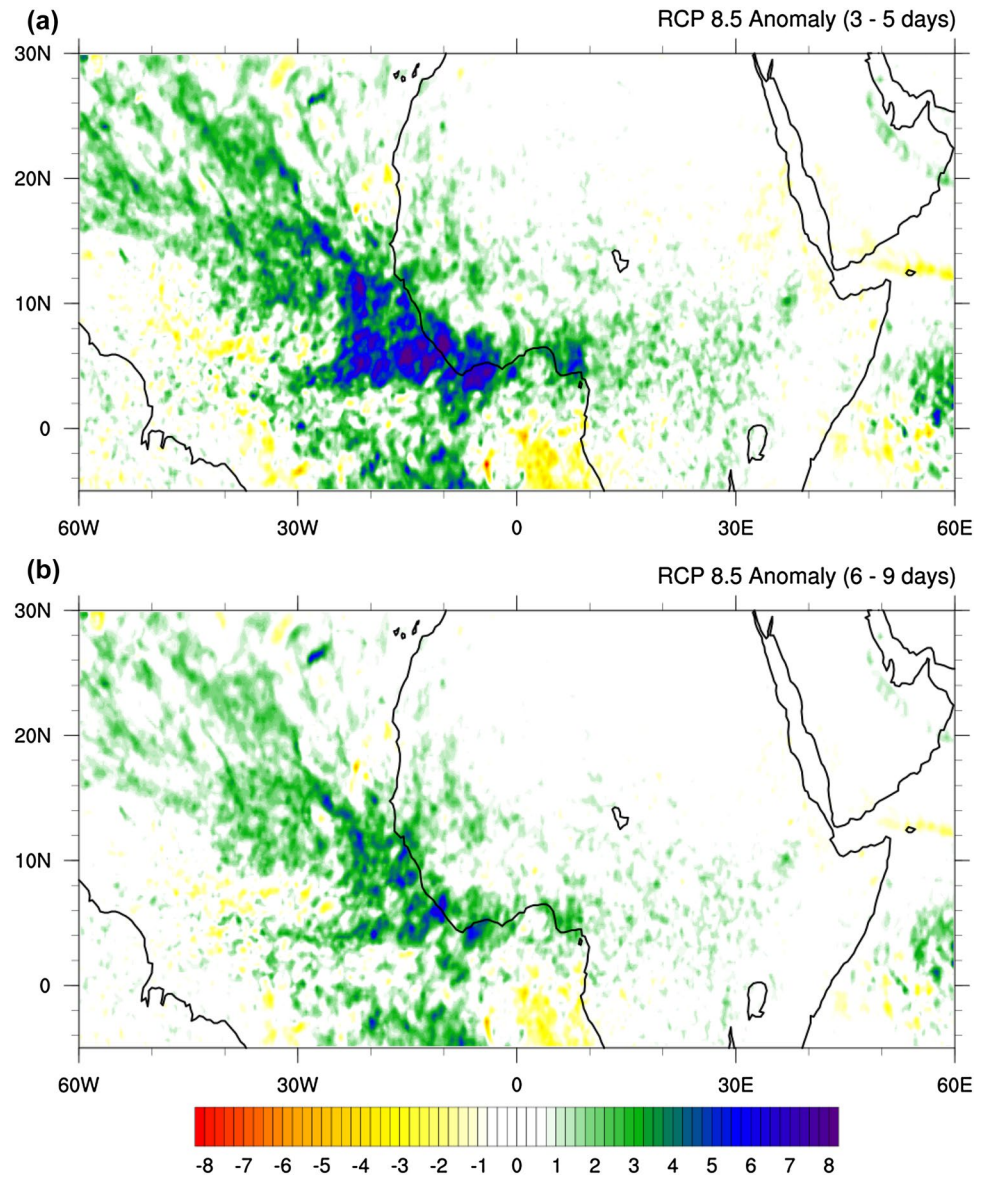
The EKE for the 6–9 day AEWs also shows an increase by the end of the twenty first century (Fig. 13b, d). As in

a smooth red noise background, from HiRAM RCP 8.5 simulation. Solid lines are dispersion curves for Kelvin, ER, MRG, and IG waves

the case of the 3–5 day AEWs, a northern oceanic region in the domain exhibits a marked increase in EKE at mid-level, whereas Western Sahara experiences a milder enhancement of EKE over the continental region (Fig. 13b). A second band of enhanced EKE ($> 2 \text{ m}^2/\text{s}^2$) is found centered over 10°N, and this enhanced AEW activity in the south might be contributing to the enhanced precipitation because this location offers a high moisture supply to the waves. This increase is less pronounced at 850 hPa, where Western Sahara and Sahel exhibit enhanced EKE up to $1.6 \text{ m}^2/\text{s}^2$ (Fig. 13d). Since the 6–9 day AEWs are formed on the northern flank of AEJ, they are mostly dry with diminished moisture supply and hence contribute less to cyclogenesis than 3–5 day AEWs. In general, the increase in EKE over the oceanic region indicates the enhanced AEW activity in this region. However it is ambiguous whether this will lead to more cyclogenesis. Previous studies have shown that seasonal variability of basin-wide hurricanes in Atlantic may not be related to AEWs (Patricola et al 2018).

To further analyze the contributing factors to the changes in EKE, different energy conversion terms are calculated. The primary energy source for eddies is available potential energy, which is then converted into kinetic energy (Lorenz 1955), and both available potential energy and kinetic energy can be separated into their mean and eddy parts. AEWs can be viewed as eddy disturbances traveling along the zonal flow, and energy conversions associated with them can be isolated into zonal mean state and eddies (Hsieh and Cook 2007). The generation of EKE in AEWs involves mainly baroclinic energy conversion, barotropic energy conversion, and diabatic heating (McCrary et al 2014). The energy

Fig. 11 Standard deviation anomalies of **a** 3–5 day and **b** 6–9 day bandpass filtered values of JJAS daily precipitation (mm/day). Anomalies are calculated as the difference between HiRAM RCP 8.5 (2080–2099) and HiRAM ESM2M (1985–2004)



conversions in AEWs can be explained using the Lorenz energy cycle. The governing equations for eddy kinetic and available potential energy in an open system are

$$\frac{\partial K_E}{\partial t} = C_k + C_{pk} - D_E + K_{EB} + \phi_{EB} \quad (1)$$

and

$$\frac{\partial A_E}{\partial t} = C_A - C_{pk} + G_E + A_{EB} \quad (2)$$

where K_E is the average eddy kinetic energy and A_E is the eddy available potential energy, C_k is barotropic energy conversion, C_{pk} is the baroclinic energy conversion term, and D_E is the frictional dissipation. The conversion term of zonal available potential energy to eddy available potential

energy due to eddy heat flux along the zonal mean temperature gradient is given by C_A , and generation of eddy available potential energy by diabatic heating is given G_E . K_{EB} and A_{EB} are the boundary fluxes of eddy kinetic and available potential energy, respectively. ϕ_{EB} is the boundary pressure work performed by the eddies.

The energy conversion terms are calculated as

$$C_k = -\overline{V_H' \cdot (\overline{V'} \cdot \nabla) V_H'} \quad (3)$$

$$C_{pk} = -\frac{R}{p} \overline{\omega' T'} \quad (4)$$

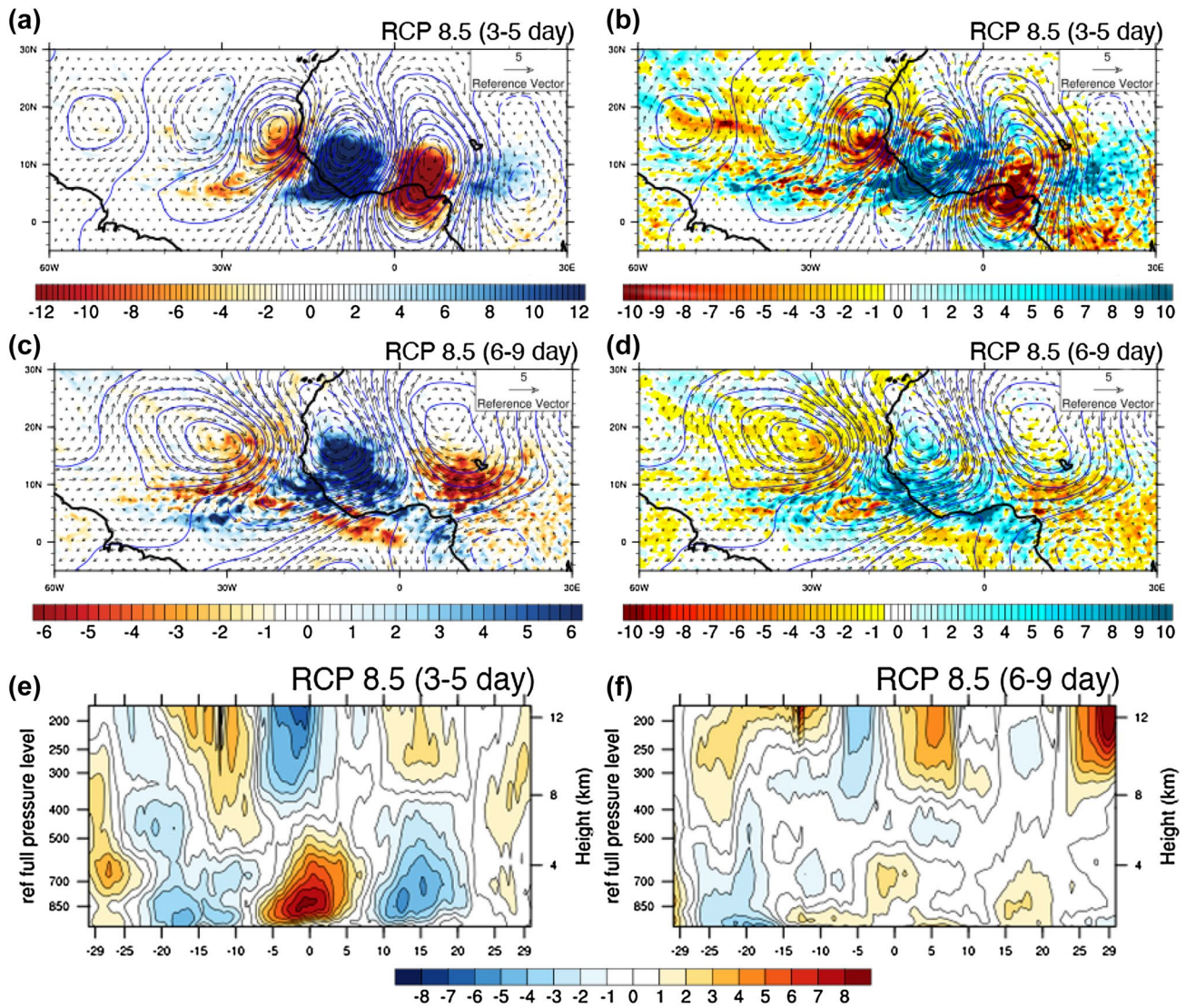


Fig. 12 a Composite anomalies of rainfall for 3–5 day AEWs on 0th day for HiRAM RCP 8.5 simulation from 2080 to 2099. Vectors are 700 hPa wind anomalies (m/s). Blue contours are the stream function. Rainfall anomalies (mm/day) are shaded, (b) the same as (a) except for the shading is the rainfall anomalies calculated as the dif-

ference between HiRAM RCP 8.5 (2080–2099) and HiRAM ESM2M (1985–2004), (c–d) same as (a–b) but for 6–9 AEWs, e meridional height cross-sections of anomaly of meridional wind (m/s) on 0th day between RCP 8.5 projections and history simulations, for 3–5 day AEWs (f) same as (e) but for 6–9 AEWs

$$C_A = -\frac{c_p \gamma}{T} \overline{V_H' T'} \cdot \nabla_H \bar{T} \tag{5}$$

$$G_E = \frac{\gamma}{T} \overline{Q_1' T'} \tag{6}$$

where T is daily mean temperature, $\omega = dp/dt$, is the vertical velocity, Q_1 is the apparent heat source, V_H is the horizontal wind speed, and p is pressure. Also, $\gamma = \frac{\Gamma_d}{\Gamma_d - \Gamma}$, where Γ_d and Γ are the dry adiabatic and observed lapse rates, respectively, c_p is the heat capacity at constant pressure, and R is the dry air gas constant.

The apparent heat source is calculated as:

$$Q_1 = \frac{c_p T}{\theta} \left(\frac{\partial \theta}{\partial t} + u \frac{\partial \theta}{\partial \phi} + v \frac{\partial \theta}{\partial \lambda} + \omega \frac{\partial \theta}{\partial p} \right) \tag{7}$$

where θ is the potential temperature.

Primes in these equations are calculated using 3–5 day and 6–9 day Butterworth bandpass filter. The higher order terms (triple products of perturbations) in (1) and (2) are omitted from analysis (Hsieh and Cook 2007). The positive and negative values in these figures represent gain and loss of EKE or eddy available potential energy respectively. The contours represent mean values from history

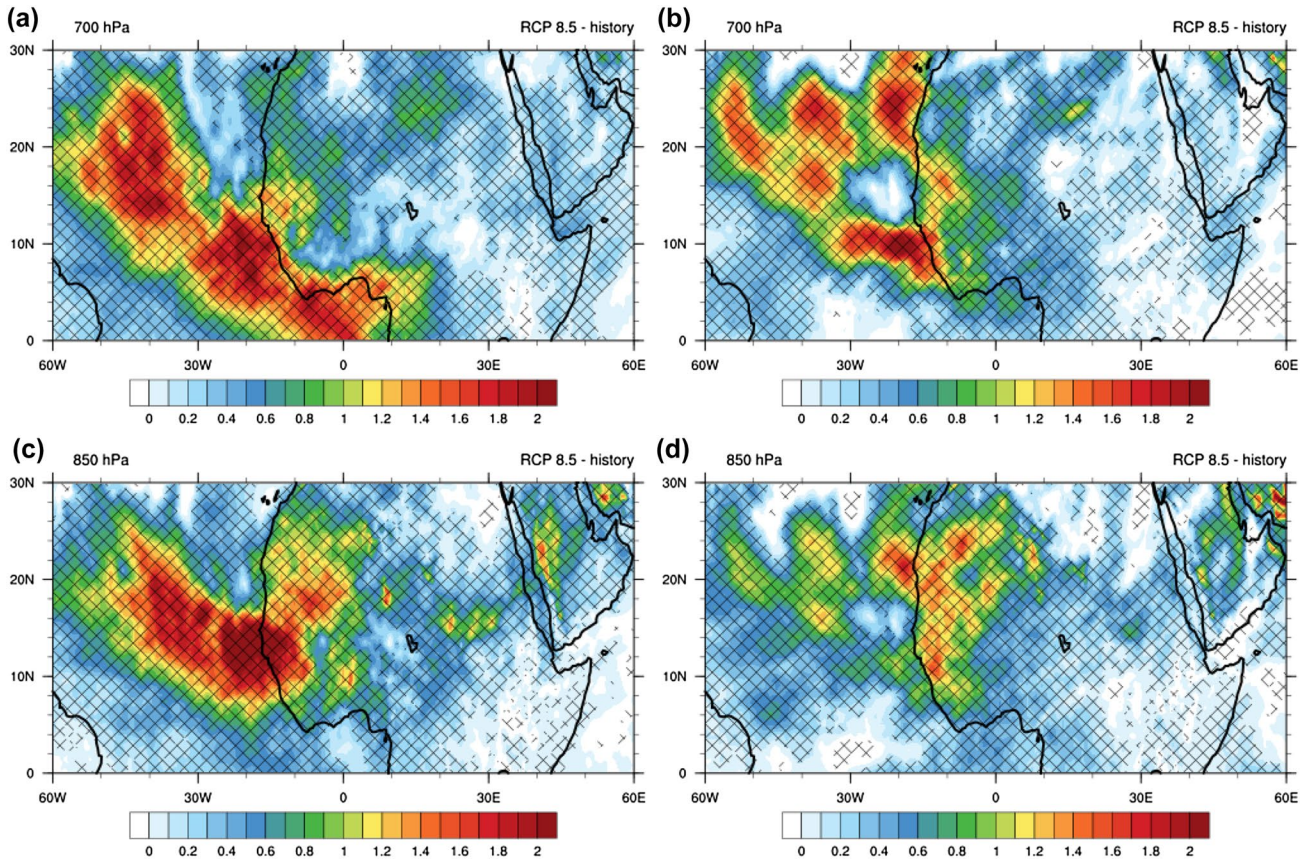


Fig. 13 EKE anomalies (m^2/s^2) from HiRAM RCP 8.5 at (a and c) 700 hPa, and (b and d) 850 hPa. Anomalies are calculated as the difference between HiRAM RCP 8.5 (2080–2099) and HiRAM ESM2M (1985–2004). The left panel is 3–5 day AEWs, whereas the

right panel is 6–9 day AEWs. The hatching indicates the areas where the anomalies are statistically significant at least at 95% confidence level. Statistical significance is calculated using Student t-test and the degrees of freedom are 2438

simulations and shades are the anomalies between history simulation and future projection.

Figure 14a, e show the meridional cross-section of the baroclinic energy conversion term ($-\frac{R}{p}\overline{\omega'T'}$) calculated from the HiRAM simulations for the 3–5 and 6–9 day AEWs, respectively. Baroclinic conversion is an important energy source for AEWs, which converts eddy available potential energy to EKE, and is associated with meridional overturning. For the 3–5 day AEWs, positive values of baroclinic conversion terms are found north of 12°N in the history simulations, and this band of positive values extends up to 700 hPa (Fig. 14a). This feature is associated with the ascending of hot dry air in the northern and descending of cold air in the southern parts of the domain (Hsieh and Cook 2007). Another band of positive baroclinic conversion is found between 500 and 200 hPa centered over 10°N , which is associated with the latent heat release from the convection in the AEWs. The latent heat release causes the ascent of warm air in these levels. Below 500 hPa, a region of negative baroclinic conversion can be seen, associated with the ascent

of cold air, which is a typical characteristic of waves (Diehliou et al 2002; Hsieh and Cook 2007). This latent heat release due to convective precipitation is a major driver of waves in the tropics (Nitta 1972). For the 3–5 day AEWs, the baroclinic conversion term in the upper troposphere is very pronounced, which could be due to the exaggerated convection in these waves in HiRAM. While the regions of positive baroclinic energy conversion are similar in the 6–9 day AEWs, their strength is less (fig. 14e). Since the convective precipitation is less in the 6–9 day AEWs, the upper troposphere latent heat release is also diminished. This is reflected in the lower values of baroclinic energy conversion at this level. Anomalies from future projections exhibit an increase in baroclinic conversion in the lower and upper troposphere for both 3–5 and 6–9 day AEWs. The increase in the upper-tropospheric baroclinic term could be due to the enhanced precipitation from waves in the future. As in the case of mean values from history simulations, future anomalies for the 3–5 day AEWs are bigger than those of the 6–9 day AEWs. A shallow band of negative anomalies over 500 hPa is seen for both waves.

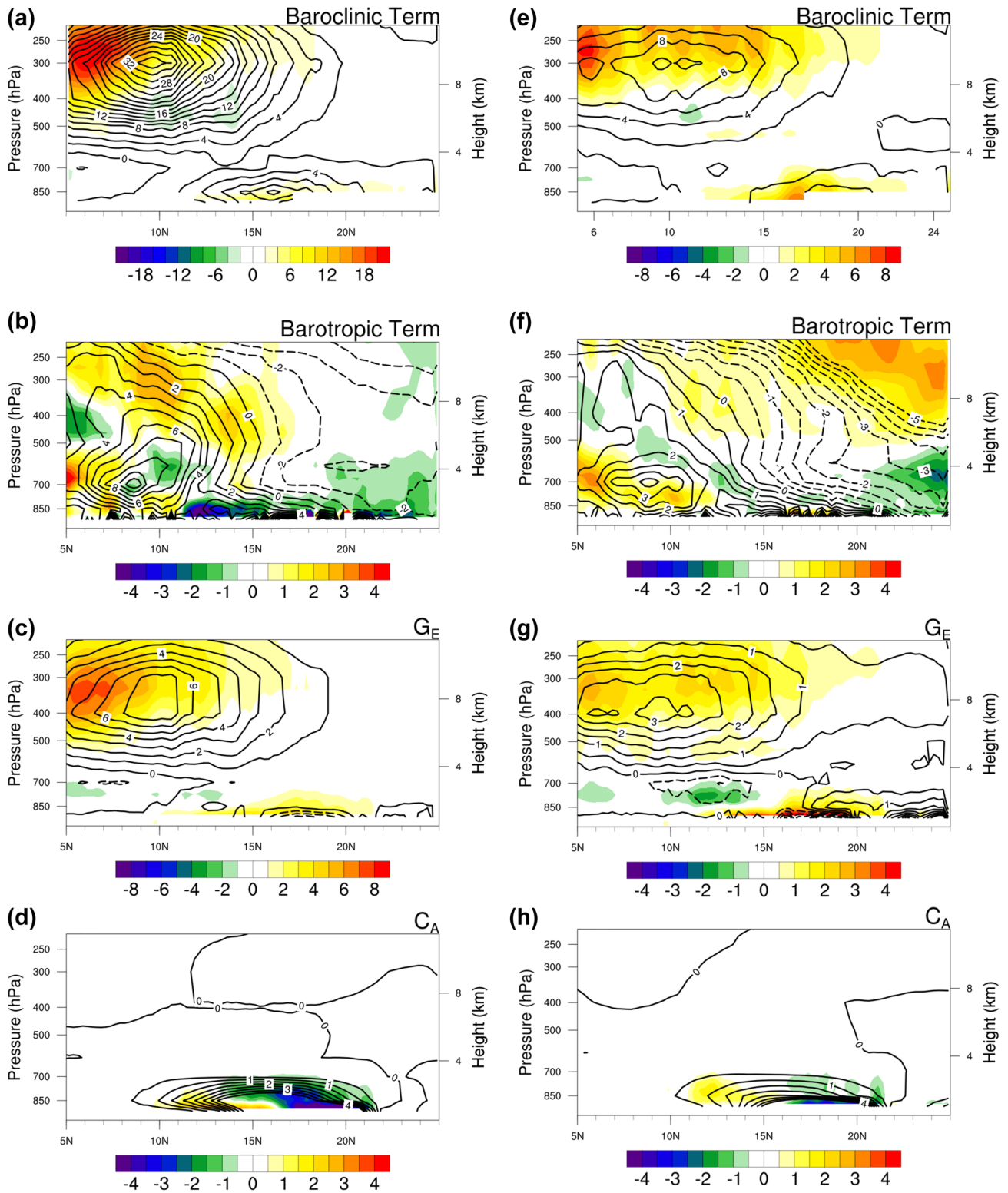


Fig. 14 Meridional height cross-sections of **(a and e)** baroclinic term, **(b and f)** barotropic term, **(c and g)** G_E and **(d and h)** C_A averaged between 20°W and 10°E . Contours represent mean values from history simulations and shades are the anomalies between history

and future simulations. Anomalies are calculated as the difference between HiRAM RCP 8.5 (2080–2099) and HiRAM ESM2M (1985–2004). The left panel is 3–5 day AEWs whereas the right panel is 6–9 day AEWs. Energy terms are in $\text{m}^2/\text{s}^2/\text{day}$

Figure 14b, f show the barotropic conversion term $(-\mathbf{V}'_{\mathbf{H}} \cdot (\nabla' \cdot \nabla) \mathbf{V}_{\mathbf{H}})$ for the 3–5 and 6–9 day AEWs, respectively. Barotropic energy conversion is the secondary source of EKE, and it converts zonal kinetic energy to EKE. For the 3–5 day waves there exist three main regions of positive mean baroclinic conversion, over the upper, middle, and lower troposphere (contours in Fig. 14b). The upper tropospheric positive values starting around 6°N are caused by anticyclonic divergent flow from the ITCZ and large shear of the tropical easterly jet (TEJ) (Hsieh and Cook 2007). The second region is in the middle troposphere and is centered over 10°N, south of AEJ. This region is associated with EKE production due to AEWs. Meanwhile, on the northern flank of AEJ, around 17.5°N, barotropic conversion has significantly lower values. This disparity in the values on either side of the jet causes the tilt of the wave axes. The third region is found in the lower troposphere in the north of the domain centered over 18°N. This is the region where the moist southwesterly monsoon winds converge with the dry Harmattan winds from the north. The positive band of barotropic conversion near tropopause is less for the 6–9 day AEWs than for their 3–5 day counterparts (Fig. 14f). The barotropic conversion associated with AEJ is well-defined for these waves, and the opposing values on either flank of the jet are similar to those in the 3–5 day AEWs. For both 3–5 and 6–9 day AEWs, a region of negative barotropic conversion, which reaches up to the tropopause, is observed, and its values are higher for the 6–9 day AEWs. The future anomalies for the 3–5 day AEWs show an increase in barotropic conversion term near the tropopause (shades in Fig. 14b). The HiRAM RCP 8.5 simulations show a stronger TEJ by the end of the century (Raj et al 2019), this could be the reason for the increase in the barotropic conversion term in this region. Interestingly, however, such an increase is not evident for the 6–9 day waves. Another region of positive anomalies extending from upper- to mid-troposphere and spanning from 10°N is seen for both types of AEWs, and this anomaly extends to the northern parts of the domain for the 6–9 day AEWs. Both types of AEWs show positive anomalies over the southern flank of AEJ, which is attributable to the increase in AEJ intensity over its southern flank in the HiRAM RCP 8.5 simulations (Raj et al 2019). Lower tropospheric barotropic conversion term anomalies exhibit a marked decrease for the 3–5 day AEWs.

Figure 14c, g show the generation term $G_E (\frac{\gamma}{T} \overline{Q'T'})$, which is a source of eddy available potential energy by means of diabatic heating. The positive value of G_E represents the generation of eddy available potential energy and is attributed to the warming of warm regions or the cooling of cold regions at the same latitude (Michaelides 1992). Meanwhile, the cooling of warm regions and warming of cold regions at the same latitudes cause the destruction of

eddy available potential energy resulting in negative values of G_E . In the mean value from history simulation, for both 3–5 and 6–9 day AEWs, the upper-tropospheric distribution of G_E and baroclinic conversion term look similar, indicating that the eddy available potential energy consumed by the baroclinic term is partially balanced by the diabatic heating (contours in Fig. 14c, g). Eddy available potential energy is generated in this region by the condensational heating from ascending warm air. G_E in this region is higher for the 3–5 day waves than the 6–9 day waves. A region of negative G_E , implying the destruction of eddy available potential energy, is found over 700 hPa for both 3–5 day (around 10°N) and 6–9 day (around 12°N) AEWs, which could be either due to ascending cold air with latent heat release or descending warm air with evaporative cooling (Hsieh and Cook 2007). A similar and stronger region of the destruction of eddy available potential energy is observed north of 15°N for both types of AEWs. Similar to the baroclinic conversion term, G_E near the tropopause exhibit an increase in the future for both types of AEWs (shades in Fig. 14c, g). The region of negative G_E near 700 hPa shows negative anomalies, which are more pronounced for the 6–9 day AEWs (Fig. 13g). Moreover, positive anomalies are seen over the lower tropospheric region of negative G_E for both the 3–5 and 6–9 day AEWs.

Figure 14d, h show the meridional cross-section of the term $C_A (-\frac{c_p \gamma}{T} \overline{\mathbf{V}'_{\mathbf{H}} T'} \cdot \nabla_H \overline{T})$, which represents the conversion of zonal available potential energy to eddy available potential energy owing to the eddy heat flux along the zonal mean temperature gradient. This is another source of eddy available potential energy which supplements the baroclinic term. A positive band of C_A values centered over 15°N is seen in the mean value from history simulation for the 3–5 day AEWs (contours in Fig. 14d). A similar region of eddy available potential energy generation is seen for the 6–9 day AEWs, but this region extends slightly more northward (Fig. 14h). In the future, this region of eddy available potential energy generation appears to be shifting toward the south (shades in Figs. 14d, h). This shift is more pronounced for the 3–5 day AEWs.

7 Summary and discussion

AEWs are the key contributors to West African rainfall and are known to act as precursors to tropical cyclones in some instances in the tropical Atlantic. Hence, predicting how AEWs will change in a warming climate is crucial for the considered region. In this study, we used a high horizontal resolution AGCM, HiRAM, to analyze future projections of AEWs. Because coarse-resolution models find it difficult to simulate AEWs and their westward propagation accurately,

mainly due to their inability to resolve the complex topography of the considered region and the parameterized convection, high-resolution models are ideal candidates to study AEWs. We used the RCP 8.5 emission scenario for future projections.

We have separated AEWs with respect to their periods, i.e., 3–5 and 6–9 day AEWs. The analysis of the zonal wavenumber–frequency power spectrum of OLR shows HiRAM successfully simulates AEWs. Further analysis of the mean evolution of wave characteristics reveals that the location, wavelength, and period of both types of simulated waves are similar to those in observations, although the precipitation is overestimated by HiRAM. The analysis of EKE shows that HiRAM overestimates, with respect to ERA5, the EKE over both low- and mid-level for both types of AEWs, although a negative bias is observed over northern Sahara at mid-level.

In general, HiRAM overestimates wave activity and the related energetics terms compared with ERA5. Because AEWs are convectively initiated and maintained waves, the difference in convective parameterization, as well as the associated condensation and vertical velocity, between HiRAM and ERA5 could be the deciding factor. HiRAM generates strong synoptic and subsynoptic variability owing to its less intrusive convective parameterization. In addition, ERA5 underestimates the synoptic-scale rainfall variability Fig. 1 and probably AEW activity.

In general, the AEW activity increases in the future, which is evident from wavenumber–frequency spectra and EKE analysis. The intensity of the circulation is also observed to increase, and the northward extent of the AEW track shows a significant increase by the end of the twenty first century. Unlike several of the previous studies mentioned in the introduction, both northern and southern track AEWs exhibit intensification in HiRAM RCP 8.5 simulation. Four energetics terms related to the generation of EKE and eddy available potential energy is calculated from both history simulation and future projection for both types of AEWs. EKE for the 3–5 day AEWs is higher than that of the 6–9 day AEWs, which is also reflected in different energetics terms. Baroclinic conversion is the main source of EKE for both types of AEWs, especially at the tropopause level. Barotropic conversion generates EKE mainly at the AEJ level. The baroclinic overturning and eddy available potential energy generated due to diabatic heating are quantitatively similar, indicating that G_E supplements the eddy available potential energy used by baroclinic conversion. This relationship becomes more pronounced in the future. Both baroclinic overturning and G_E exhibit strong positive anomalies at the tropopause level in the future, indicating enhanced latent heat release and convective heating.

It has been shown that 10%–20% of the dust entrainment over northern Africa and 10%–20% of dust variability over the tropical Atlantic is associated with AEWs (Jones et al

2003). Therefore, the future enhancement in AEW activities have implications for the dust loading over north Africa and Saharan air layer. The enhanced oceanic extent of EKE to the tropical Atlantic may also have implications in the cyclogenesis in Atlantic basin. But it is also noteworthy that AEWs are not a deciding factor in the frequency of basin-wide seasonal Atlantic cyclones (Patricola et al 2018). More studies are needed to analyze whether the cyclogenesis from AEWs shows any significant change in the future.

Supplementary Information The online version contains supplementary material available at <https://doi.org/10.1007/s00382-023-06720-y>.

Acknowledgements We thank V. Ramaswamy, M. Zhao, B. Wyman, and C. Kerr of GFDL for their assistance with acquiring and using the HiRAM model. The research reported in this publication was supported by funding from King Abdullah University of Science and Technology (KAUST). For computer time, this research used the resources of the KAUST Supercomputing Laboratory, Thuwal, Saudi Arabia. The ERA Interim data used in this work can be found at ECMWF website (<https://www.ecmwf.int/en/forecasts/datasets/reanalysis-datasets/era-interim>) and the HiRAM model source code is available at the GFDL website (<https://www.gfdl.noaa.gov/hiram-quickstart/>). The initial and boundary conditions and other data needed to reproduce the simulations are publicly available at KAUST Repository (<https://repository.kaust.edu.sa/handle/10754/660938>).

Open Access This article is licensed under a Creative Commons Attribution 4.0 International License, which permits use, sharing, adaptation, distribution and reproduction in any medium or format, as long as you give appropriate credit to the original author(s) and the source, provide a link to the Creative Commons licence, and indicate if changes were made. The images or other third party material in this article are included in the article's Creative Commons licence, unless indicated otherwise in a credit line to the material. If material is not included in the article's Creative Commons licence and your intended use is not permitted by statutory regulation or exceeds the permitted use, you will need to obtain permission directly from the copyright holder. To view a copy of this licence, visit <http://creativecommons.org/licenses/by/4.0/>.

References

- Adler RF, Sapiano MR, Huffman GJ (2018) The global precipitation climatology project (gpcp) monthly analysis (new version 2.3) and a review of, et al (2017) global precipitation. *Atmosphere* 9(4):138
- Albignat JP, Reed RJ (1980) The origin of african wave disturbances during phase iii of gate. *Mon Weather Rev* 108(11):1827–1839
- Bangalath HK, Stenchikov G (2015) Role of dust direct radiative effect on the tropical rainbelt over middle east and north africa: a high resolution agcm study. *J Geophys Res Atmos* 120:4564–4584. <https://doi.org/10.1002/2015JD023122>
- Bangalath HK, Stenchikov G (2016) Sensitivity of the middle east-north african tropical rainbelt to dust shortwave absorption: a high-resolution agcm experiment. *J Clim* 29(19):7103–7126
- Barbe LL, Lebel T (1997) Rainfall climatology of the hapex-sahel region during the years 1950–1990. *J Hydrol* 188–189:43–73. [https://doi.org/10.1016/S0022-1694\(96\)03154-X](https://doi.org/10.1016/S0022-1694(96)03154-X)
- Berry GJ, Thorncroft C (2005) Case study of an intense african easterly wave. *Mon Weather Rev* 133(4):752–766. <https://doi.org/10.1175/MWR2884.1>
- Berry GJ, Thorncroft CD (2012) African easterly wave dynamics in a mesoscale numerical model: the upscale role of

- convection. *J Atmos Sci* 69(4):1267–1283. <https://doi.org/10.1175/JAS-D-11-099.1>
- Boyle J, Klein SA (2010) Impact of horizontal resolution on climate model forecasts of tropical precipitation and diabatic heating for the TWP-ICE period. *J Geophys Res* 115:D23113. <https://doi.org/10.1029/2010JD014262>
- Brannan AL, Martin ER (2019) Future characteristics of african easterly wave tracks. *Clim Dyn* 52(9):5567–5584
- Bretherton CS, McCaa JR, Grenier H (2004) A new parameterization for shallow cumulus convection and its application to marine subtropical cloud-topped boundary layers. Part i: description and 1d results. *Mon Weather Rev* 132(4):864–882
- Burpee RW (1972) The origin and structure of easterly waves in the lower troposphere of north Africa. *J Atmos Sci* 29(1):77–90
- Burpee RW (1974) Characteristics of north African easterly waves during the summers of 1968 and 1969. *J Atmos Sci* 31(6):1556–1570
- Carlson TN (1969) Synoptic histories of three African disturbances that developed into Atlantic hurricanes. *Mon Weather Rev* 97(3):256–276
- Chen TC (2006) Characteristics of African easterly waves depicted by ecmwf reanalyses for 1991–2000. *Mon Weather Rev* 134(12):3539–3566. <https://doi.org/10.1175/MWR3259.1>
- Crétat J, Vizy EK, Cook KH (2015) The relationship between African easterly waves and daily rainfall over west Africa: observations and regional climate simulations. *Clim Dyn* 44(1):385–404. <https://doi.org/10.1007/s00382-014-2120-x>
- D’Amato N, Lebel T (1998) On the characteristics of the rainfall events in the sahel with a view to the analysis of climatic variability. *Int J Climatol* 18(9):955–974. [https://doi.org/10.1002/\(SICI\)1097-0088\(199807\)18:9<955::AID-JOC236>3.0.CO;2-6](https://doi.org/10.1002/(SICI)1097-0088(199807)18:9<955::AID-JOC236>3.0.CO;2-6)
- De Felice P, Monkam D, Viltard A et al (1990) Characteristics of north African 6–9 day waves during summer 1981. *Mon Weather Rev* 118(12):2624–2633
- Dee D, Uppala S, Simmons A et al (2011) The era-interim reanalysis: configuration and performance of the data assimilation system. *Q J R Meteorol Soc* 137(656):553–597
- Diedhiou A, Janicot S, Viltard A et al (1998) Evidence of two regimes of easterly waves over west Africa and the tropical Atlantic. *Geophys Res Lett* 25(15):2805–2808. <https://doi.org/10.1029/98GL02152>
- Diedhiou A, Janicot S, Viltard A et al (2002) Energetics of easterly wave disturbances over west Africa and the tropical Atlantic: a climatology from the 1979–95 ncep/ncar reanalyses. *Clim Dyn* 18(6):487–500. <https://doi.org/10.1007/s00382-001-0195-7>
- Dunne JP, John JG, Adcroft AJ et al (2012) Gfdl’s esm2 global coupled climate-carbon earth system models. Part i: Physical formulation and baseline simulation characteristics. *J Clim* 25(19):6646–6665
- Dunne JP, John JG, Shevliakova E et al (2013) Gfdl’s esm2 global coupled climate-carbon earth system models. Part ii: carbon system formulation and baseline simulation characteristics. *J Clim* 26(7):2247–2267
- Duvel JP (1990) Convection over tropical Africa and the Atlantic ocean during northern summer. Part ii: modulation by easterly waves. *Mon Weather Rev* 118(9):1855–1868
- Estoque M, Lin M (1977) Energetics of easterly waves. *Mon Weather Rev* 105(5):582–589
- Fink AH, Reiner A (2003) Spatiotemporal variability of the relation between African easterly waves and west African squall lines in 1998 and 1999. *J Geophys Res Atmos*. <https://doi.org/10.1029/2002JD002816>
- Fink AH, Vincent DG, Ermert V (2006) Rainfall types in the west African sudanian zone during the summer monsoon 2002. *Mon Weather Rev* 134(8):2143–2164. <https://doi.org/10.1175/MWR3182.1>
- Gamdt G (2004) The new GFDL global atmosphere and land model am2-lm2: evaluation with prescribed SST simulations. *J Clim* 17:4641–4673. <https://doi.org/10.1175/JCLI-3223.1>
- Gent PR, Yeager SG, Neale RB et al (2010) Improvements in a half degree atmosphere/land version of the ccsm. *Clim Dyn* 34(6):819–833
- Ginoux P, Horowitz LW, Ramaswamy V et al (2006) Evaluation of aerosol distribution and optical depth in the geophysical fluid dynamics laboratory coupled model cm2. 1 for present climate. *J Geophys Res Atmos* (1984–2012). <https://doi.org/10.1029/2005JD006707>
- Gray WM (1968) Global view of the origin of tropical disturbances and storms. *Mon Weather Rev* 96(10):669–700. [https://doi.org/10.1175/1520-0493\(1968\)096<0669:GVOTOO>2.0.CO;2](https://doi.org/10.1175/1520-0493(1968)096<0669:GVOTOO>2.0.CO;2)
- Gu G, Adler RF, Huffman GJ et al (2004) African easterly waves and their association with precipitation. *J Geophys Res Atmos*. <https://doi.org/10.1029/2003JD003967>
- Hamilton H, Núñez Ocasio K, Evans J et al (2020) Topographic influence on the African easterly jet and African easterly wave energetics. *J Geophys Res Atmos* 125(8):e2019JD032
- Hannah WM, Aiyyer A (2017) Reduced African easterly wave activity with quadrupled co2 in the superparameterized cesm. *J Clim* 30(20):8253–8274. <https://doi.org/10.1175/JCLI-D-16-0822.1>
- Hersbach H, Bell B, Berrisford P et al (2020) The era5 global reanalysis. *Q J R Meteorol Soc* 146(730):1999–2049
- Hopsch SB, Thorncroft CD, Hodges K et al (2007) West African storm tracks and their relationship to Atlantic tropical cyclones. *J Clim* 20(11):2468–2483. <https://doi.org/10.1175/JCLI4139.1>
- Horowitz LW, Walters S, Mauzerall DL et al (2003) A global simulation of tropospheric ozone and related tracers: description and evaluation of Mozart, version 2. *J Geophys Res Atmos* (1984–2012). <https://doi.org/10.1029/2002JD002853>
- Hou AY, Kakar RK, Neeck S et al (2014) The global precipitation measurement mission. *Bull Am Meteor Soc* 95(5):701–722
- Hsieh JS, Cook KH (2007) A study of the energetics of African easterly waves using a regional climate model. *J Atmos Sci* 64(2):421–440. <https://doi.org/10.1175/JAS3851.1>
- Jones C, Mahowald N, Luo C (2003) The role of easterly waves on African desert dust transport. *J Clim* 16(22):3617–3628
- Kebe I, Diallo I, Sylla MB et al (2020) Late 21st century projected changes in the relationship between precipitation, African easterly jet, and African easterly waves. *Atmosphere* 11(4):353
- Kiladis GN, Thorncroft CD, Hall NMJ (2006) Three-dimensional structure and dynamics of African easterly waves. Part I: observations. *J Atmos Sci* 63(9):2212–2230. <https://doi.org/10.1175/JAS3741.1>
- Landsea CW (1993) A climatology of intense (or major) Atlantic hurricanes. *Mon Weather Rev* 121(6):1703–1713. [https://doi.org/10.1175/1520-0493\(1993\)121<1703:ACOIMA>2.0.CO;2](https://doi.org/10.1175/1520-0493(1993)121<1703:ACOIMA>2.0.CO;2)
- Lau NC, Ploshay JJ (2009) Simulation of synoptic-and subsynoptic-scale phenomena associated with the east Asian summer monsoon using a high-resolution GCM. *Mon Weather Rev* 137(1):137–160
- Laurent H, D’Amato N, Lebel T (1998) How important is the contribution of the mesoscale convective complexes to the sahelian rainfall. *Phys Chem Earth* 23(5):629–633. [https://doi.org/10.1016/S0079-1946\(98\)00099-8](https://doi.org/10.1016/S0079-1946(98)00099-8)
- Leroux S, Hall NMJ, Kiladis GN (2010) A climatological study of transient-mean-flow interactions over west Africa. *Q J R Meteorol Soc* 136(S1):397–410. <https://doi.org/10.1002/qj.474>
- Lin SJ (2004) A “vertically lagrangian” finite-volume dynamical core for global models. *Mon Weather Rev* 132(10):2293–2307. [https://doi.org/10.1175/1520-0493\(2004\)132](https://doi.org/10.1175/1520-0493(2004)132)
- Lorenz EN (1955) Available potential energy and the maintenance of the general circulation. *Tellus* 7(2):157–167
- Manganello JV, Hodges KI, Kinter JL et al (2012) Tropical cyclone climatology in a 10-km global atmospheric GCM: toward

- weather-resolving climate modeling. *J Clim* 25(11):3867–3893. <https://doi.org/10.1175/JCLI-D-11-00346.1>
- Mariotti L, Diallo I, Coppola E et al (2014) Seasonal and intraseasonal changes of African monsoon climates in 21st century cordex projections. *Clim Change* 125(1):53–65
- Martin ER, Thorncroft C (2015) Representation of African easterly waves in cmip5 models. *J Clim* 28(19):7702–7715. <https://doi.org/10.1175/JCLI-D-15-0145.1>
- Mathon V, Diedhiou A, Laurent H (2002) Relationship between easterly waves and mesoscale convective systems over the sahel. *Geophys Res Lett* 29(8):57–1
- McCrary RR, Randall DA, Stan C (2014) Simulations of the west African monsoon with a superparameterized climate model. Part II: African easterly waves. *J Climate* 27(22):8323–8341
- Mekonnen A, Thorncroft CD, Aiyyer AR (2006) Analysis of convection and its association with African easterly waves. *J Clim* 19(20):5405–5421
- Michaelides SC (1992) A spatial and temporal energetics analysis of a baroclinic disturbance in the Mediterranean. *Mon Weather Rev* 120(7):1224–1243
- Nitta T (1972) Energy budget of wave disturbances over the Marshall islands during the years of 1956 and 1958. *J Meteorol Soc Japan Ser II* 50(2):71–84
- Norquist DC, Recker EE, Reed RJ (1977) The energetics of African wave disturbances as observed during phase iii of gate. *Mon Weather Rev* 105(3):334–342
- Pasch RJ, Avila LA, Jiing JG (1998) Atlantic tropical systems of 1994 and 1995: a comparison of a quiet season to a near-record-breaking one. *Mon Weather Rev* 126(5):1106–1123. [https://doi.org/10.1175/1520-0493\(1998\)126<1106:ATSOAA>2.0.CO;2](https://doi.org/10.1175/1520-0493(1998)126<1106:ATSOAA>2.0.CO;2)
- Patricola CM, Saravanan R, Chang P (2018) The response of Atlantic tropical cyclones to suppression of African easterly waves. *Geophys Res Lett* 45(1):471–479
- Putman WM, Lin SJ (2007) Finite-volume transport on various cubed-sphere grids. *J Comput Phys* 227(1):55–78. <https://doi.org/10.1016/j.jcp.2007.07.022>
- Pytharoulis I, Thorncroft C (1999) The low-level structure of African easterly waves in 1995. *Mon Weather Rev* 127(10):2266–2280. [https://doi.org/10.1175/1520-0493\(1999\)127<2266:TLLSOA>2.0.CO;2](https://doi.org/10.1175/1520-0493(1999)127<2266:TLLSOA>2.0.CO;2)
- Raj J, Bangalath HK, Stenchikov G (2019) West African monsoon: current state and future projections in a high-resolution agcm. *Clim Dyn* 52(11):6441–6461. <https://doi.org/10.1007/s00382-018-4522-7>
- Redelsperger JL, Diongue A, Diedhiou A et al (2002) Multi-scale description of a sahelian synoptic weather system representative of the west African monsoon. *Q J R Meteorol Soc* 128(582):1229–1257. <https://doi.org/10.1256/003590002320373274>
- Reed RJ, Norquist DC, Recker EE (1977) The structure and properties of African wave disturbances as observed during phase iii of gate. *Mon Weather Rev* 105(3):317–333
- Reed RJ, Klinker E, Hollingsworth A (1988) The structure and characteristics of African easterly wave disturbances as determined from the ecmwf operational analysis/forecast system. *Meteorol Atmos Phys* 38(1):22–33. <https://doi.org/10.1007/BF01029944>
- Rennick MA (1976) The generation of African waves. *J Atmos Sci* 33(10):1955–1969
- Russell JO, Aiyyer A, White JD et al (2017) Revisiting the connection between African easterly waves and Atlantic tropical cyclogenesis. *Geophys Res Lett* 44(1):587–595
- Skinner CB, Diffenbaugh NS (2014) Projected changes in African easterly wave intensity and track in response to greenhouse forcing. *Proc Nat Acad Sci* 111(19):6882–6887. <https://doi.org/10.1073/pnas.1319597111>
- Thorncroft C, Hodges K (2001) African easterly wave variability and its relationship to Atlantic tropical cyclone activity. *J Clim* 14(6):1166–1179. [https://doi.org/10.1175/1520-0442\(2001\)014<1166:AEWVAI>2.0.CO;2](https://doi.org/10.1175/1520-0442(2001)014<1166:AEWVAI>2.0.CO;2)
- Thorncroft C, Hoskins B (1994) An idealized study of African easterly waves. I: a linear view. *Q J R Meteorol Soc* 120(518):953–982
- Thorncroft C, Hoskins B (1994) An idealized study of African easterly waves ii: a nonlinear view. *Q J R Meteorol Soc* 120(518):983–1015
- Trenberth KE, Stepaniak DP, Hurrell JW et al (2001) Quality of reanalyses in the tropics. *J Clim* 14(7):1499–1510. [https://doi.org/10.1175/1520-0442\(2001\)014<1499:QORITT>2.0.CO;2](https://doi.org/10.1175/1520-0442(2001)014<1499:QORITT>2.0.CO;2)
- Wehner MF, Reed KA, Li F et al (2014) The effect of horizontal resolution on simulation quality in the community atmospheric model, cam5. 1. *J Adv Model Earth Syst* 6(4):980–997
- Wheeler M, Kiladis GN (1999) Convectively coupled equatorial waves: analysis of clouds and temperature in the wavenumber-frequency domain. *J Atmos Sci* 56(3):374–399. [https://doi.org/10.1175/1520-0469\(1999\)056<0374:CCEWAO>2.0.CO;2](https://doi.org/10.1175/1520-0469(1999)056<0374:CCEWAO>2.0.CO;2)
- Wu MLC, Reale O, Schubert SD (2013) A characterization of African easterly waves on 2.5–6-day and 6–9-day time scales. *J Clim* 26(18):6750–6774. <https://doi.org/10.1175/JCLI-D-12-00336.1>
- Zhao M, Held IM, Lin SJ et al (2009) Simulations of global hurricane climatology, interannual variability, and response to global warming using a 50-km resolution gcm. *J Clim* 22(24):6653–6678. <https://doi.org/10.1175/2009JCLI3049.1>

Publisher's Note Springer Nature remains neutral with regard to jurisdictional claims in published maps and institutional affiliations.